

RESEARCH ARTICLE

Improved regional forecasting of an extreme Arctic cyclone in August 2016 with WRF MRI-4DVAR

Junmei Ban¹ | Zhiquan Liu¹  | David H. Bromwich²  | Lesheng Bai²

¹National Center for Atmospheric Research, Boulder, Colorado, USA

²Polar Meteorology Group, Byrd Polar and Climate Research Center, The Ohio State University, Columbus, Ohio, USA

Correspondence

David H. Bromwich, Byrd Polar and Climate Research Center, 1090 Carmack Road, Columbus, OH, USA.
Email: bromwich.1@osu.edu

Funding information

Office of Naval Research, Grant/Award Numbers: N00014-18-1-2361, N00014-21-1-2650

Abstract

Cycling data assimilation and forecast experiments in August 2016 together with a case study of an intense Arctic cyclone (AC16) are performed. Initial conditions from newly developed Multi-Resolution Incremental Four-Dimensional Variational (MRI-4DVAR) and Three-Dimensional Variational (3DVAR) data assimilation along with forecasts from the polar version of the Weather Research and Forecasting (Polar WRF) model, mimicking operational configurations, are applied. The tasks are to evaluate MRI-4DVAR performance during a 20-day cycling run, to investigate the impacts of initial conditions on the forecast skill of AC16, and to identify the factors impacting AC16's predictability. The results from the 20-day cycling period demonstrate the robustness and reliability of MRI-4DVAR for data assimilation and subsequent forecast skill. Multiple processes, including mergers of Arctic cyclones, mergers of vortices, vertical coupling between low-level and upper-level circulations, baroclinic processes and jet stream forcing, contributed to the generation and development of AC16. Compared to the initial conditions from 4DVAR, 3DVAR produced amplified polar vortices, stronger baroclinic instability, intensified upper-level jet streams and a stronger low-level frontal zone, causing the overdevelopment of AC16 in 3DVAR-based forecasts. For MRI-4DVAR, the accurate prediction of AC16 5–7 days ahead is likely due primarily to the more accurate representation of upper-level atmospheric fields, that was facilitated by better satellite radiance assimilation with MRI-4DVAR that also produced a balanced initial model state. It is concluded that the high-resolution Polar WRF which is optimized for Arctic conditions combined with 4DVAR facilitated the improved prediction of AC16 compared to the Global Forecast System (GFS) operational deterministic global forecast.

KEYWORDS

data assimilation, forecasting, MRI-4DVAR, summer Arctic cyclone

1 | INTRODUCTION

Arctic Cyclones (ACs) are one of the most important synoptic systems in high-latitude weather and climate (Simmonds *et al.*, 2008; Inoue, 2021), and can be associated with high winds, extreme waves, heavy precipitation, and reduced visibility. In summer, these impacts adversely affect human activity, especially the commercial use of Arctic sea routes (Yamagami *et al.*, 2018a, 2018b; De Silva and Yamaguchi, 2019; Inoue, 2021). Hence it is important to provide timely and accurate predictions of ACs. Yamagami *et al.* (2018a) picked 10 “extraordinary” summer ACs whose central pressure was lower than 980 hPa from 2008 to 2016 and investigated their predictability using operational medium-range ensemble forecasts from five centers, namely the Canadian Meteorological Center (CMC), European Centre for Medium-Range Weather Forecasts (ECMWF), Japan Meteorological Agency (JMA), the US National Centers for Environmental Prediction (NCEP), and the UK Met Office (UKMO). They pointed out that the central position of the extraordinary ACs can be forecasted accurately 3.5 days prior to the mature stage with a positional displacement of 300–500 km and a central pressure biased high by 6–11 hPa. In addition, Yamagami *et al.* (2018b) examined the medium-range ensemble forecast skill for the Great Arctic Cyclone in August 2012 (AC12) and found similar predictive skill.

Skillful prediction of ACs can be facilitated by using a well-performing data assimilation (DA) system that provides accurate initial conditions. Four-dimensional variational (4DVAR) DA is one of the most advanced approaches. In 4DVAR, observations can be assimilated at their appropriate measurement times with the constraint of the tangent-linear and adjoint model (TLM/ADM, Errico *et al.*, 1993; Errico, 1997; Errico and Raeder, 1999) of the non-linear forecast model, which permits the proper propagation of information over the assimilation window with flow-dependent background error covariances (Laroche *et al.*, 2007). Despite these advantages, the applications of 4DVAR are limited by its expensive computational cost especially when using a high-resolution configuration.

Most operational centers, such as ECMWF (Rabier *et al.*, 2000), UKMO (Rawlins *et al.*, 2007), JMA (Kadowaki, 2005), Météo-France (Gauthier and Thépaut, 2001) and Meteorological Service of Canada (MSC; Gauthier *et al.*, 2007), implemented 4DVAR with the incremental formulation (Courtier *et al.*, 1994) to reduce its computational cost. The incremental approach allows the use of different grid spacing for calculating the background departure in outer loops (at full model resolution) and performing minimization in inner iterations (at lower resolution). Simplified TLM/ADM physics parameterizations

Significance Statement

Intense summer cyclones disrupt the sea ice cover of the Arctic Ocean and are an important factor in its continuing demise. These cyclones can be challenging to forecast more than three days in advance. This study employs a regional forecast model optimized for Arctic conditions in conjunction with an advanced method to produce starting conditions for the model prediction. A highly accurate cyclone forecast was obtained five days ahead with forecast skill continuing for a further two days. It appears that accurate forecasts of these dangerous and destructive weather events of the Arctic Ocean can be anticipated for up to a week in advance.

can be used in inner-loop minimization to reduce the computational cost further. The Weather Research and Forecasting (WRF) (Skamarock *et al.*, 2008) model's 4DVAR (Huang *et al.*, 2009) also adopts the incremental formulation but can do inner-loop minimization only at the full model resolution with its released code on and prior to version 4.2. Liu *et al.* (2020) (hereafter referred to as Liu20) extended WRF 4DVAR to allow the minimization to be performed at lower resolutions for inner iterations, with the analysis increment interpolated from low to high resolution and then being added to the high-resolution first guess. It is referred to as the Multi-Resolution Incremental 4DVAR (MRI-4DVAR), which leads to a substantial speed-up and was applied to an afternoon thunderstorm case over northern Taiwan with a 2-km model grid spacing (Liu20) and a record-breaking rainstorm case in Guangzhou, China with a 3-km grid-spacing setting (Wu *et al.*, 2020), respectively. Promising results were obtained with WRF MRI-4DVAR for these two convective-scale applications with a relatively short time window (30 min).

This study applies WRF Data Assimilation (WRFDA) MRI-4DVAR to ACs, a large-scale phenomenon, with a six-hour assimilation time window. Twenty-day cycling experiments with 15-km grid spacing are conducted to evaluate the stability, robustness, and performance of MRI-4DVAR. The selected period includes an extreme AC on 16 August 2016 (hereafter, AC16) that initiated a major decrease in the sea ice cover (Lukovich *et al.*, 2021). In addition to statistical measures of forecast performance over the 20-day cycling runs, the skill in predicting the extreme AC16 with MRI-4DVAR is also investigated to determine whether this event can be better predicted than the GFS deterministic forecast.

The outline of the paper is as follows: a synoptic analysis of the extreme Arctic cyclone evolution is given in Section 2. The Polar WRF model configuration, MRI-4DVAR DA procedure, assimilated observations, and experimental design are described in Section 3. Section 4

presents the results from the 20-day cycling run and the AC16 case study, followed by the conclusion in Section 5.

2 | SYNOPTIC OVERVIEW OF THE EXTREME ARCTIC CYCLONE IN AUGUST 2016

In 2016, an extreme Arctic cyclone (i.e., AC16) was recorded at 0000 UTC on 16 August (Yamagami *et al.*, 2017) and it had a significant impact on the Arctic environment. AC16 was of similar size and intensity to AC12 (Yamagami *et al.*, 2017). We chose the time period of August 2016 to evaluate the stability, robustness, and performance of MRI-4DVAR. Furthermore, the prediction of AC16 is investigated in detail.

At high latitudes, it is vortices rather than waves that govern the dynamics (Hakim, 2000). Tropopause Polar Vortices (TPVs) (Cavallo and Hakim, 2009, 2010) can play an important role in the development and maintenance of Arctic cyclones via upper-level potential vorticity forcing (Gray *et al.*, 2021) on the Eurasian side of the Arctic where AC16 developed. TPVs are of mesoscale to synoptic scale in contrast to the much larger scale polar vortex (e.g., Gray *et al.*, 2021); this terminology is adopted here for the summer although recognizing there are differing opinions on this matter. TPVs are identified in terms of local minima in potential temperature (θ , unit: K) on the dynamic tropopause (Hakim and Canavan, 2005), here analyzed on the commonly used 2-potential vorticity unit (2-PVU) surface, and local maxima of potential vorticity on isobaric surfaces.

Figures 1–3 illustrate the temporal evolution of AC16 from the perspective of lower-and upper-atmospheric fields from the NCEP Global Forecast System (GFS) analysis. On 0000 UTC 11 August 2016 (Figures 1a and 2a), the features of interest were three marked surface cyclones AC1, AC2, AC3 along with a weak low AC4, three TPVs, TPV1, TPV3, TPV4 (where the number corresponds to the name of the associated surface cyclone), and the quasi-stationary polar vortex over the Arctic Ocean (PV) in the troposphere and stratosphere. All these labels are unique to this manuscript because we want to focus on the factors contributing to the development of the mature AC16. For analysis of the evolution of AC16, the baroclinicity, polar vortex, jet stream and TPV effects on the storm development are investigated according to the different stages of development of AC16.

2.1 | Initial stage

On 11 August (Figure 1a), a frontal zone, revealed by the 850-hPa temperature gradient, was located south of the

Scandinavian Mountains and AC1 developed on this feature. Figure 1f shows the geographic features mentioned in the text along with the tracks of cyclones AC1 and AC3. TPV1 located over the Norwegian Sea was accompanied to the east by a strong upper-level jet stream (Figure 2a) whose right entrance favored the development of AC1. AC2 developed over the Laptev Sea originally on 4 August and was maintained for more than one month (Yamagami *et al.*, 2017). The structure of AC2 was barotropic without a frontal zone or jet stream but was vertically coupled with the polar vortex PV (Figure 3a). AC3 was a mature cyclone with a very weak frontal zone and supported by TPV3. AC4 over the Laptev Sea was a weak low linked to TPV4 (Figure 2a).

On 12 August (Figure 1b), the frontal zone strengthened and extended to the southwestern Barents Sea and synoptic-scale frontal cyclone AC1 intensified over the Barents Sea. TPV1 moved eastward and began to influence AC1 (Figure 3b). The structure of AC1 was similar to a midlatitude cyclone; it was accompanied and forced by TPV1 and indirect circulation associated with the strong upper-level jet stream (Figure 2b). Meanwhile, AC3 and TPV3 moved northnortheast from the Kara Sea to the Arctic Ocean (Figures 1b and 3c). AC4 and TPV4 merged respectively into AC2 and the polar vortex PV (Figure 1b), and this first merger enhanced PV with the 500-hPa heights dropping from 517 to 514 dam.

On 13 August (Figures 1c and 2c), AC1 developed into a typical baroclinic cyclone with warm and cold fronts in its initial development stage and had a warm core at upper levels and a cold core at low levels (Figure 3d). The accompanying upper-level jet stream moved northeastward and strengthened (Figure 2c). Two wind speed maxima of this jet stream can be seen with AC1 developing in the favored location between them (Tao *et al.*, 2017a) and the second maximum was close to the center of PV, starting to enhance it. At the same time, AC3 merged into AC2 and TPV3 merged into the polar vortex PV (Figure 1c). The merging process and the forcing of the jet stream further enhanced the polar vortex PV, with the central 500-hPa geopotential height dropping from 514 dam on the 12th to 511 dam on the 13th, and the central pressure of AC2 decreased from 997 to 988 hPa as a result of combining with AC3 (Figure 1c).

2.2 | Early development stage

From 13 to 14 August (Figures 1d and 2d), AC1 moved northeastward from the Barents Sea to the Kara Sea (Figure 1d,f) and developed rapidly, with the central pressure of AC1 dropping 13 hPa from 998 to 985 hPa.

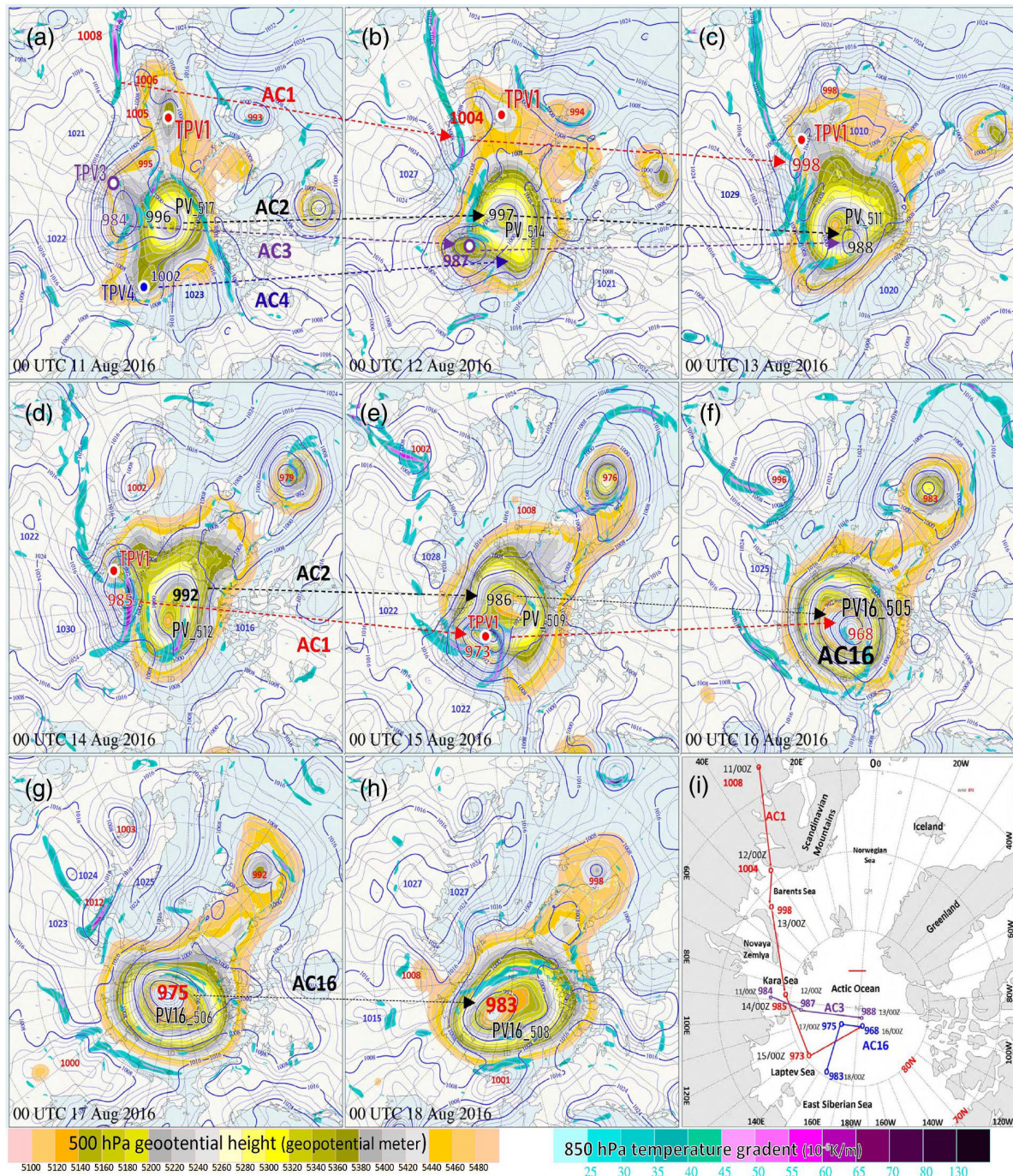


FIGURE 1 (a–h): 850 hPa temperature gradient (shaded), sea level pressure (contour interval is 2 hPa in dark blue), and 500 hPa geopotential height (contour interval is 20 m shaded) from the global forecast system analysis at 0000 UTC on 11–18 August 2016. The red, black, purple and blue arrow lines show the tracks of AC1, AC2, AC3 and AC4 respectively. Ocean areas are colored light blue. Tropopause Polar Vortex-1 (TPV1), (●), TPV3 (○) and TPV4 (●) show the high level locations of TPVs. Latitudes, longitudes, and geographic names mentioned in this paper are marked in (i). The track of Cyclones AC1, AC3 and AC16 at every 0000 UTC are marked in (i). [Colour figure can be viewed at wileyonlinelibrary.com]

The AC1 fronts started to occlude, and AC1 approached maturity. The upper-level jet stream moved northeastward to the Arctic Ocean. The AC1 center was located close to TPV1 and between the two jet streaks, suggesting that the cyclone was still developing baroclinically.

2.3 | Rapid intensification stage

From 14 to 15 August (Figures 1e and 2e), AC1 continued to develop rapidly and moved to the Laptev Sea; the central pressure dropped 12 hPa from 985 to 973 hPa,

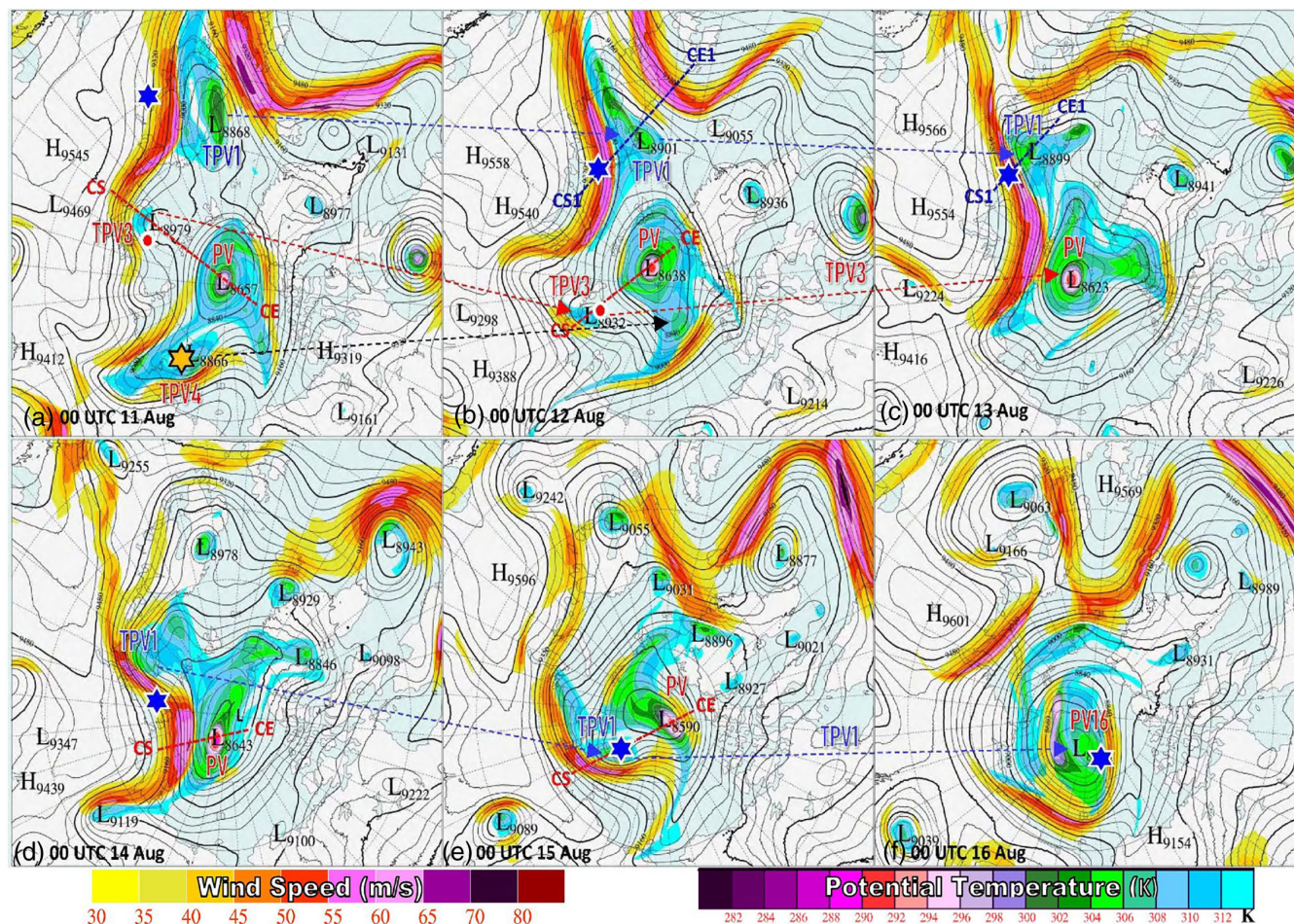


FIGURE 2 Global Forecast System analysis of 300 hPa geopotential height (contour interval is 40 m in black), and potential temperature (K, shaded) and wind speed ($\text{m}\cdot\text{s}^{-1}$, shaded) on the 2-potential vorticity unit surface. The blue, red and black dashed arrow lines show the tracks of Tropopause Polar Vortex-1 (TPV1), TPV3 and TPV4 respectively. The dashed lines indicate the cross-sections from CS (CS1) to CE (CE1) in Figure 3. The symbols show the center location of cyclones AC1 (★), AC3 (●) and AC4 (☆). [Colour figure can be viewed at wileyonlinelibrary.com]

and its fronts continued to occlude. TPV1 substantially intensified (central value at 500 hPa decreased from 531 to 513 dam, Figure 1e), moved eastnortheastward to the Arctic Ocean, and vertically coupled with AC1 (Figure 3f). The upper-level jet stream weakened and was still connected with AC1 and TPV1, but it was removed from the polar vortex PV (Figure 2e). AC2 deepened continuously with the central pressure dropping 6 hPa from 992 to 986 hPa. The polar vortex PV intensified (central value decreased from 512 to 509 dam) and moved northward to the center of the Arctic Ocean.

2.4 | Later development stage

From 15 to 16 August, AC1 merged with AC2 to form AC16) and TPV1 merged with PV to form PV16; the central pressure decreased 5 hPa from 973 to 968 hPa, the low-level system coupled with upper-level polar

vortex, and an axisymmetric vertical structure developed (Figure 1f). After the merging of the cyclones and vortices (Figure 1g,h), the fronts and jet stream became separated from the center of AC16 and AC16 exhibited a barotropic structure, indicating that baroclinicity was not the primary energy source and barotropic forcing played an important role in the later phase of its development. In the dissipating stage from 16 to 18 August, AC16 weakened, and the central pressure rose to 975 hPa on 17 August and 983 hPa on 18 August, and it kept an axisymmetric vertical structure. These stages are used to discuss the impact of data assimilation on the forecasts of AC16 in Section 4.3.

To summarize, multiple processes contributed to the generation and development of AC16. In the initial phase, AC4 and TPV4 (AC3 and TPV3) merged into AC2 and the polar vortex PV on 12 (13) August. With both mergers AC2 and PV were intensified. The baroclinic growth of AC1 (low-level front, upper-level jet stream and TPV1)

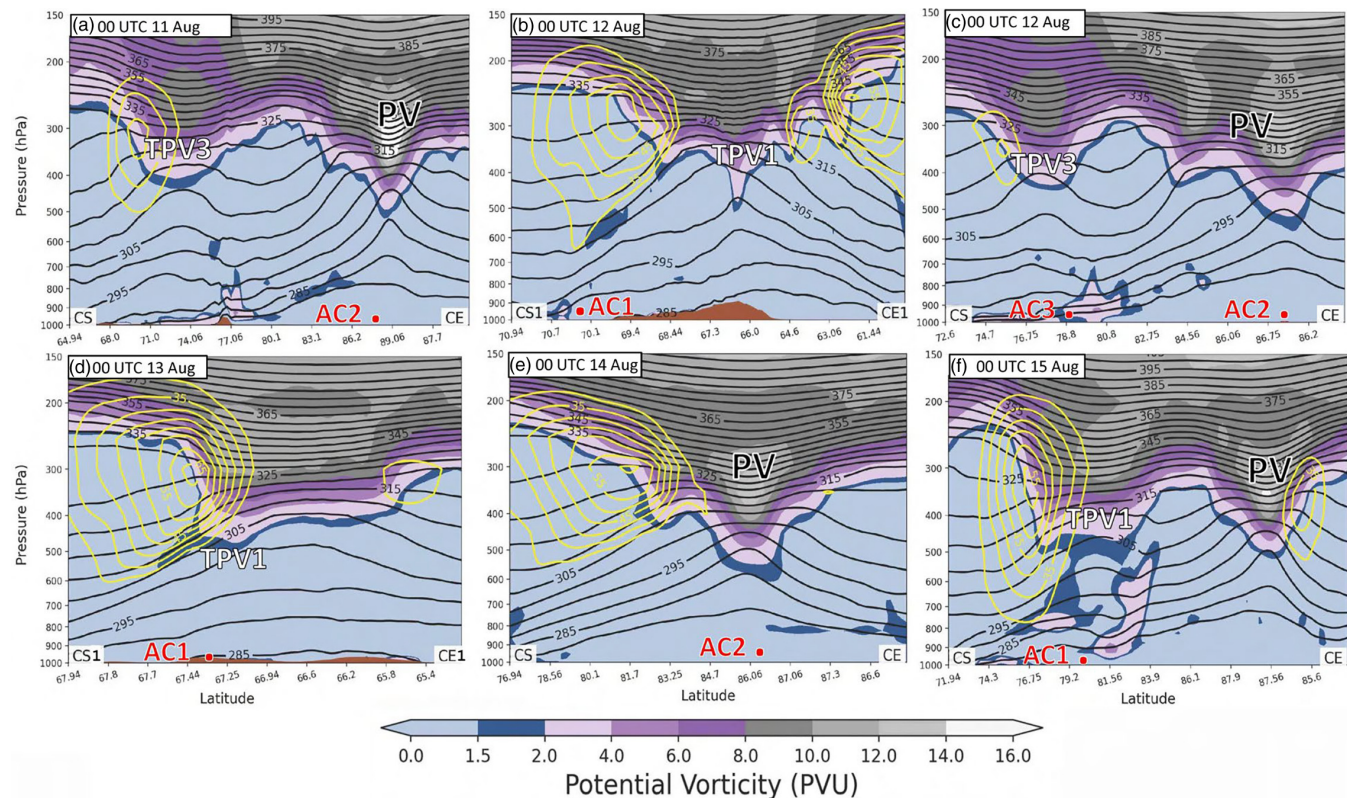


FIGURE 3 Cross-sections of potential vorticity (PVU, shaded), potential temperature (K, contour interval is 5 K in black) and wind speed ($\text{m}\cdot\text{s}^{-1}$, contour interval is 5 $\text{m}\cdot\text{s}^{-1}$ in yellow and the range is from 30 to 70 $\text{m}\cdot\text{s}^{-1}$) from the Global Forecast System analysis. Cyclone center is marked in red dot if the cross-section passes through the cyclone center. Terrain is in brown. Cross-sections are along the colored dashed lines in Figure 2. [Colour figure can be viewed at wileyonlinelibrary.com]

from 11 to 15 August and the merging of AC1 with AC2 from 15 to 16 August that enhanced the polar vortex were a non-linear baroclinic and barotropic development via the low-level system coupling with the upper polar vortex.

3 | MODEL CONFIGURATION, OBSERVATIONS AND EXPERIMENTAL DESIGN

3.1 | Polar WRF model configurations

The polar-optimized version of the WRF model (Polar WRF, e.g., Bromwich *et al.*, 2009) is used in this study. Simulations are conducted with Polar WRF version 4.1.1, which includes the improved representation of heat transfer through snow and ice (Hines and Bromwich, 2008; Hines *et al.*, 2015). Physical parameterizations used here are based upon previous experience with Polar WRF applications (e.g., Bromwich *et al.*, 2009; Hines *et al.*, 2011; Wilson *et al.*, 2011; Steinhoff *et al.*, 2013). They are the Morrison two-moment microphysics scheme (Morrison *et al.*, 2009), the Kain–Fritsch cumulus parameterization (Kain, 2004), the Rapid Radiative Transfer

Model for GCMs longwave and shortwave radiation schemes (Mlawer *et al.*, 1997; Iacono *et al.*, 2008), the Mellor–Yamada–Nakanishi–Niino 2.5-level planetary boundary layer (Nakanishi, 2001; Nakanishi and Niino, 2004, 2006), and the Noah Land Surface Model (Chen and Dudhia, 2001). Figure 4a shows the computational domain. The grid spacing is 15 km (613×613 grid points). The model top is at 10 hPa and there are 57 vertical levels with the first level at about 8 m above the surface.

3.2 | WRF MRI-4DVAR

MRI-4DVAR (Liu20) based on the WRF Data Assimilation (WRFDA, Barker *et al.*, 2012) V4.1.1 is used in this study. Liu20 provided mathematical formulation and implementation details of MRI-4DVAR and thus we only provide a brief description of MRI-4DVAR here. Different from the normal full-resolution WRF 4DVAR, MRI-4DVAR uses a three-stage procedure controlled by scripts and offline programs, including observer, minimizer, and regridding. The observer step runs WRFDA to compute the first-guess departure from the observations using the full-resolution nonlinear model (NLM)

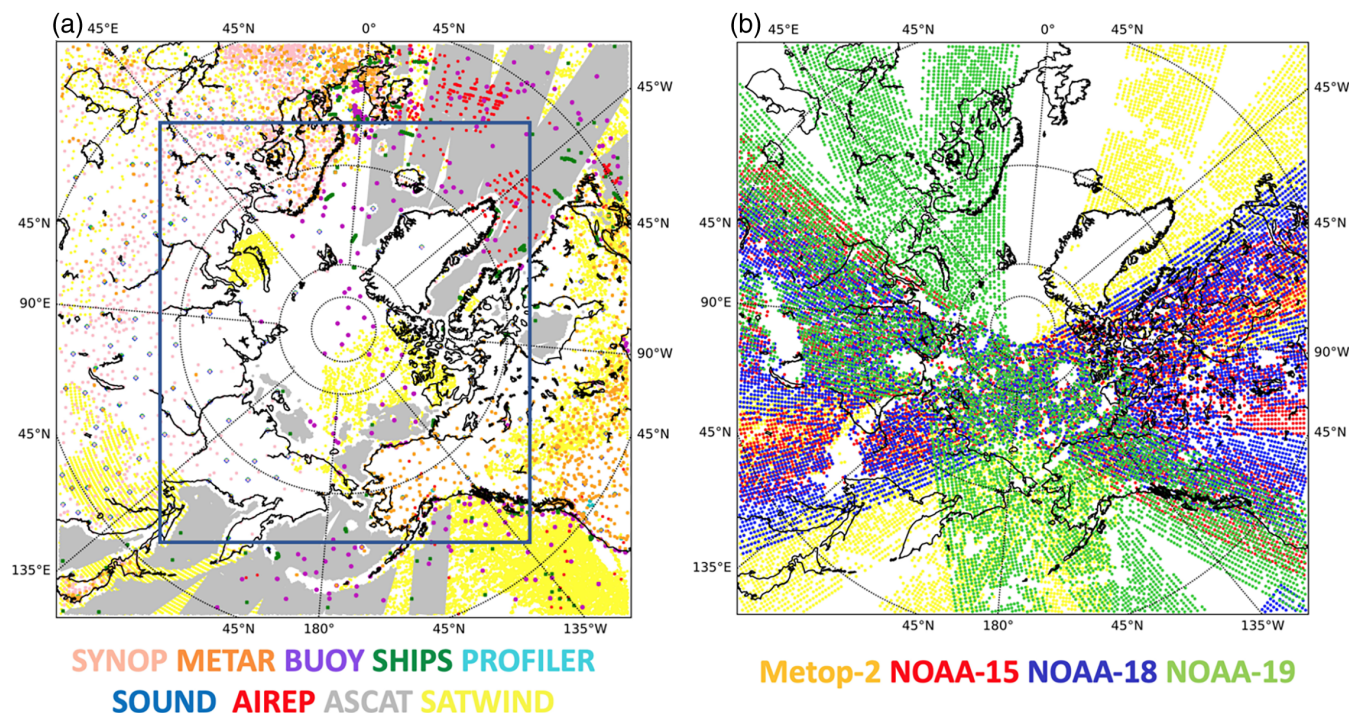


FIGURE 4 Model domain and a snapshot of (a) conventional observation distributions and (b) Advanced Microwave Sounding Unit A radiance data coverage which is thinned on the 60-km grid from four satellites within a six-hour time window centered at 0000 UTC 2 August 2016. The smaller domain within the blue box (a) is used for model space verification against the Global Forecast System analysis. Observation space verification is performed for latitudes greater than 60° N. [Colour figure can be viewed at wileyonlinelibrary.com]

trajectory within the time window and writes out the first-guess departure to files on disk. The minimizer step runs WRFDA to perform inner iterations at a lower resolution using the first-guess departure computed in the observer step. The regridding step runs offline programs to interpolate the low-resolution analysis increment to the full resolution and add it to the full-resolution background, which forms the full-resolution analysis for the use of the observer step of the next outer loop. One key element of WRF MRI-4DVAR is the introduction of inverse control variable transforms in the minimizer step within WRFDA, which is part of the procedure of converting empirical orthogonal functions space control variables from low resolution to high resolution of the next outer loop.

3.3 | Observations

Conventional in situ data and satellite-derived winds from the Global Telecommunications System (GTS) are assimilated in this study. Surface data include surface pressure, temperature and specific humidity at 2 m, and u-wind and v-wind components at 10 m from synoptic weather stations (SYNOP) and airport stations (METAR) over land, and also from buoys (BUOY) and ships (SHIPS) over the ocean. Upper-air data consist of

u-wind and v-wind from profilers (PROFILER), u-wind, v-wind, temperature and specific humidity from radiosondes (SOUND), and u-wind, v-wind and temperature from aircraft (AIREP). Two types of satellite-derived products are assimilated, including 10-m ocean surface winds from the Advanced SCATterometer (ASCAT) and upper-air u-wind and v-wind components of satellite cloud-track wind products retrieved from polar-orbiting and geostationary satellites (SATWIND). Figure 4a shows that there is no coverage over the Arctic Ocean for radiosonde and profiler data. Aircraft reports are mainly over the Atlantic and do not reach latitudes north of 70° N. The drifting buoys are scattered over the Arctic Ocean and are mainly located north of Greenland and Canada with some of them reaching 87° N.

Advanced Microwave Sounding Unit A (AMSU-A) (Goodrum *et al.*, 1999) radiances from NOAA-15, -18, -19 and METOP-2 satellites are also assimilated. Considering snow/sea ice coverage over the Arctic region and the 10-hPa model top, window channels (1–4 and 15) and high-peaking channels (10–14) are not assimilated in this study. Therefore, only temperature-sensitive channels 5–9 are assimilated. Figure 4b shows the locations of assimilated AMSU-A radiances. The model domain is well covered by more than three orbits of each satellite within the six-hour time window.

3.4 | Experimental design

Three experiments, termed 3DVAR, 135km45km MRI-4DVAR, and 45km45km MRI-4DVAR, are performed in a continuously cycling configuration over a 20-day period beginning from 0600 UTC of 1 August 2016. All the three experiments use a six-hour cycling interval with a six-hour assimilation time window centered at four analysis times at 0000/0600/1200/1800 UTC. The background of each analysis is a six-hour forecast from the previous cycle, except for the first analysis at 0600 UTC of 1 August that uses a six-hour forecast from the GFS analysis at 0000 UTC of 1 August. To reduce the impact of large-scale drift at the upper levels during the 20-day continuous cycling, especially for 3DVAR, we apply spectral nudging for horizontal wind, potential temperature, and geopotential height in six-hour intervals above model level 40 (100 hPa) on all three experiments. For the seven-day free forecasts which are initialized from each 0000 UTC analysis, we do not apply nudging. To mimic an operational configuration in real time, the lateral boundary conditions for WRF forecasts are provided by the GFS operational deterministic forecasts in six-hour intervals.

For the 3DVAR experiment, all observations are assumed to be valid at the center of the six-hour assimilation window. The maximum number of inner iterations (at the full model resolution of 15 km) is set to 70 in 3DVAR, but for most cycles the cost function and gradient norm converged before 40 iterations. Two MRI-4DVAR experiments are performed with two outer loops having lower-resolution inner iterations at the minimizer step: 135km45km uses 135 km inner-loop resolution (69×69 grid points) for the first outer loop and 45 km (205×205 grid points) for the second outer loop whereas 45km45km uses 45 km inner-loop resolution for both outer loops. Note that the departure of observations from the NLM background trajectory within the six-hour time window is performed at the full model resolution of 15 km. Considering its computational cost, the maximum number of inner iterations is set to 25 for the two MRI-4DVAR experiments. Observations within the six-hour 4DVAR time window are divided into hourly time slots (30 min for the beginning and end of the time window). Other 4DVAR-related settings are similar to those of Liu20 with the use of TLM/ADM of simplified physics schemes.

For the two MRI-4DVAR experiments, one should ensure that the corresponding inner-loop resolution model terrain is used for the integration of TLM and ADM in the minimizer step as mentioned in Liu20. The background error covariance files needed for 3DVAR and MRI-4DVAR are generated at 15, 45, and 135 km grid spacing respectively using the National Meteorological Center (NMC) method (Parrish and Derber, 1992). All experiments

assimilate conventional observations and AMSU-A radiances as described in Section 3.3. For radiance assimilation, the Community Radiative Transfer Model (CRTM; Han *et al.*, 2006) is used as the radiance forward operator, and radiances over both land and ocean are assimilated. The variational bias correction (Auligné *et al.*, 2007) is utilized for radiance assimilation. The background check is applied as part of the quality control, in which an observation is rejected if its innovation (i.e., observation minus background) exceeds three times the observation error standard deviation. The dense AMSU-A radiance data can have spatially correlated observation errors (Liu and Rabier, 2002), which are not taken into account in WRFDA. Therefore, the AMSU-A radiances are thinned on a 60-km grid to reduce the error correlation.

4 | RESULTS

4.1 | Computational efficiency of MRI-4DVAR

Experiments are conducted on the Ohio Supercomputer Center's (OSC) Owens Cluster that consists of 824 nodes with 28 cores and 128 GB memory per node. The wall-clock times for the three experiments and each step of the three-stage MRI-4DVAR are given in Table 1. It should be noted that only one node can be used for 135 km minimization on Owens Cluster. The wall-clock time will be further reduced if we can use more nodes. While the process could have been sped up by using more nodes, about 70 min wall-clock time for the 135km45km setting and about 90 min wall-clock time for the 45km45km setting are reasonable for a real-time application with a forecast lead time of seven days.

4.2 | 20-day cycling diagnostics

In this subsection, 20-day cycling MRI-4DVAR and 3DVAR experiments are verified in both observation and model space to evaluate the stability, robustness, and performance.

4.2.1 | Departure statistics

The observation minus background (OMB) statistics are used to evaluate the assimilation performance for the cycling run poleward of 60° N. Figure 5a depicts the time series of root mean square (RMS) of OMB for the ASCAT ocean surface wind observations from 3DVAR. The RMS of OMB from the 3DVAR fluctuated

TABLE 1 Wall-clock times of three experiments with six-hour assimilation time window on the OSC HPC computing system

Experiments		Grid points	Processors	Wall-clock time	
3DVAR		613 × 613	280	3 min	
135km45km	15 km get innovation	613 × 613	280	10 min	~70 min (time consumed for thinning and regridding in serial run added)
	135 km minimisation	69 × 69	20	17 min	
	45 km minimisation	205 × 205	280	35 min	
45km45km	15 km get innovation	613 × 613	280	10 min	~90 min (time consumed for thinning and regridding in serial run added)
	45 km minimisation	205 × 205	280	35 min	
	45 km minimisation	205 × 205	280	35 min	

Note: For MRI-4DVAR, the costs of each step are also listed. Note: the total wall-clock time for MRI-4DVAR also includes time consumed for thinning from high-resolution guess to low-resolution and regridding increment from low-resolution to high-resolution.

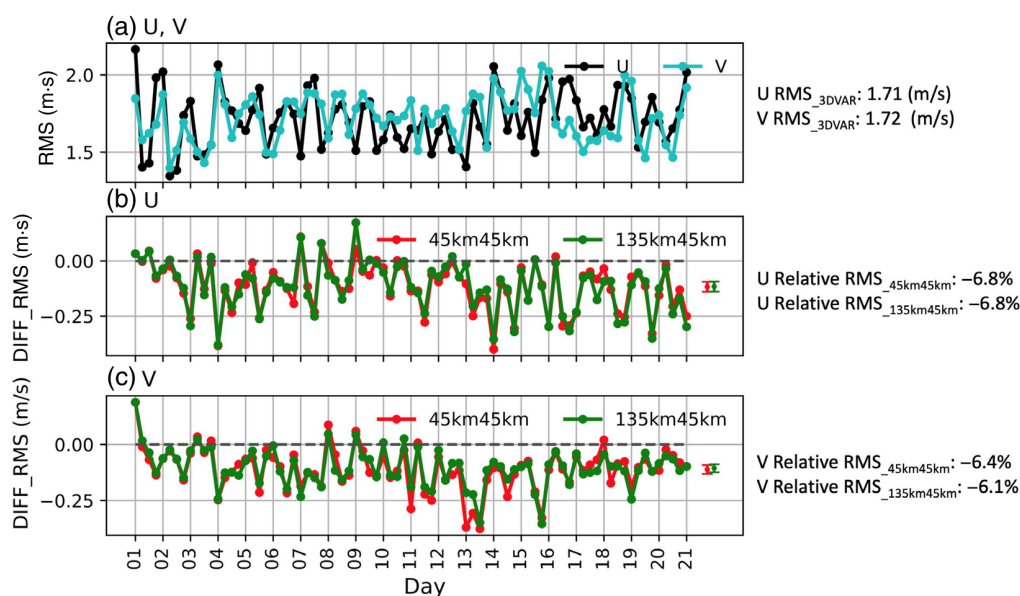


FIGURE 5 (a) Time series of root mean square (RMS) ($\text{m}\cdot\text{s}^{-1}$) of observation minus background (OMB) for Advanced SCATterometer ocean surface winds from the experiment 3DVAR for u and v. (b) RMS differences between the MRI-4DVAR experiments and 3DVAR for u. (c) is same as (b), but for v. The right-most points with vertical bar in (b) and (c) show the RMS differences aggregated over 81 samples for the cycling period, and the vertical bar shows 95% confidence interval after 8,000 bootstrap resamplings. (a–c) share the same x-axis. The values of RMS and relative RMS are listed on the right side of the figure. [Colour figure can be viewed at wileyonlinelibrary.com]

between 1.3 and $2.2\text{ m}\cdot\text{s}^{-1}$, and the average RMS for u (v) is 1.71 (1.72) $\text{m}\cdot\text{s}^{-1}$ in the cycling period. To investigate the MRI-4DVAR's performance compared to 3DVAR, Figure 5b,c show the RMS differences between MRI-4DVAR and 3DVAR, and the negative (positive) values indicate improvement (degradation) over 3DVAR. For most of the time, the RMS differences are negative, indicating MRI-4DVAR has smaller RMS errors than 3DVAR. For the average RMS differences over 81 samples which are shown on the right in green (135km45km) and red (45km45km), there is no zero-value included in the confidence interval, so the improvements for u- and v-wind components are statistically significant for

the MRI-4DVAR experiments. The relative reduction of RMS is adopted to compare quantitatively between 3DVAR experiment and MRI-4DVAR experiments: $\text{relative RMS} = 100\%(\text{RMS}_{\text{MRI-4DVAR}} - \text{RMS}_{\text{3DVAR}})/\text{RMS}_{\text{3DVAR}}$. Compared with 3DVAR, the RMS error from 135km45km (45km 45km) decreases 6.8% (6.8%) for the u-wind component and decreases 6.1% (6.4%) for the v-wind component.

The positive impact of MRI-4DVAR can also be seen when we use radiance observations to check the upper-level OMB statistics. The brightness temperature from NOAA-15 AMSU-A channel 8 is used, whose weighting function peaks around 150 hPa. Figure 6a shows the RMS of brightness temperature from 3DVAR fluctuated

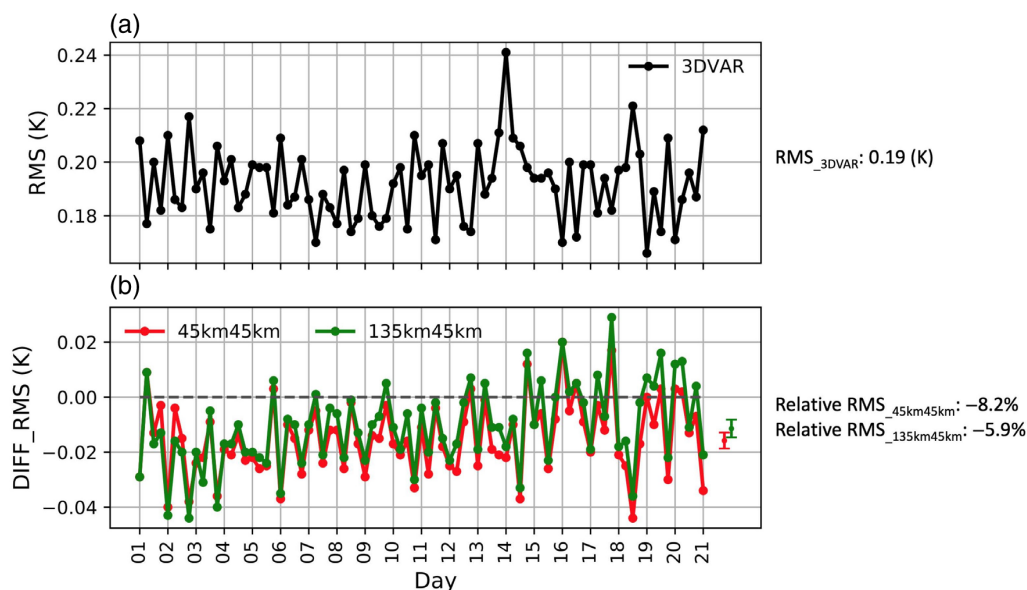


FIGURE 6 (a) Time series of root mean square (RMS) (K) of brightness temperature observation minus background (OMB) from the experiment 3DVAR relative to NOAA-15 Advanced Microwave Sounding Unit A channel 8. (b) RMS differences between the MRI-4DVAR experiments and 3DVAR. The right-most points with vertical bar in (b) show the RMS differences averaged over 81 samples during the cycling period, and the vertical bars show 95% confidence interval after 8,000 bootstrap resamplings. (a) and (b) share the same x-axis. The values of RMS and relative RMS are listed on the right side of the figure. [Colour figure can be viewed at wileyonlinelibrary.com]

between 0.16 and 0.24 K during the cycling period. Compared with 3DVAR, the RMS error from 135km45km (45km45km) decreases 5.9% (8.2%). The RMS reductions of MRI-4DVAR relative to 3DVAR are statistically significant.

4.2.2 | Forecast verification

Figure 7 shows bias from the three experiments and RMS differences of six-hour to seven-day surface pressure (P_s) forecasts when verified against the GFS analysis over all cycles initialized from 20 forecast samples at 0000 UTC. For bias, the P_s from all the three forecast runs is generally more negative than the GFS analysis by up to 1.3 hPa for the day-7 forecast of 3DVAR. A nearly constant bias reduction of 0.4 hPa compared to 3DVAR is achieved for most forecast lead times from 45km45km. A further about 0.1-hPa bias reduction is seen from 135km45km for lead times beyond 2.5 days. For root mean square error (RMSE), the greater improvements from the two MRI-4DVAR runs are mainly for forecast lead times less than two days and beyond five days with a 4%–10% RMS error reduction.

To examine the upper-air forecast of MRI-4DVAR, the RMS differences between 3DVAR and 4DVAR with respect to GFS analyses are displayed in Figure 8 for forecasts at 12 hours and seven days. For the 12-hr forecasts, the most pronounced improvement from the two 4DVAR

experiments is for the geopotential height (Z) field when compared to 3DVAR. The relative improvement in RMS of Z varied from about 5% to about 35% at different levels. Thus, 45km45km 4DVAR is better than 135km45km 4DVAR, but not statistically different. Consistent 4DVAR improvement relative to 3DVAR for Z forecasts lasts to day-7 with an about 7% RMS reduction around 900 hPa. Two MRI-4DVAR experiments have also an overall positive impact on wind and temperature fields, but with a smaller magnitude than that of Z . There is a degradation in MRI-4DVAR in the temperature field at the lowest levels and wind field between 250 and 400 hPa at 12 hours, which turn into neutral or positive impacts at day-7.

Although the focus of this study is the forecast performance of AC16, these statistical measures over the whole 20-day cycling period indicate robustness and good performance of WRF MRI-4DVAR, which has been developed recently with room for further improvement and tuning for better skill.

4.3 | Case study of extreme Arctic cyclone in August 2016

4.3.1 | Surface forecasts and cloud predictions

In this subsection, we evaluate the forecasts initialized from 0000 UTC 11 August 2016 for different aspects of

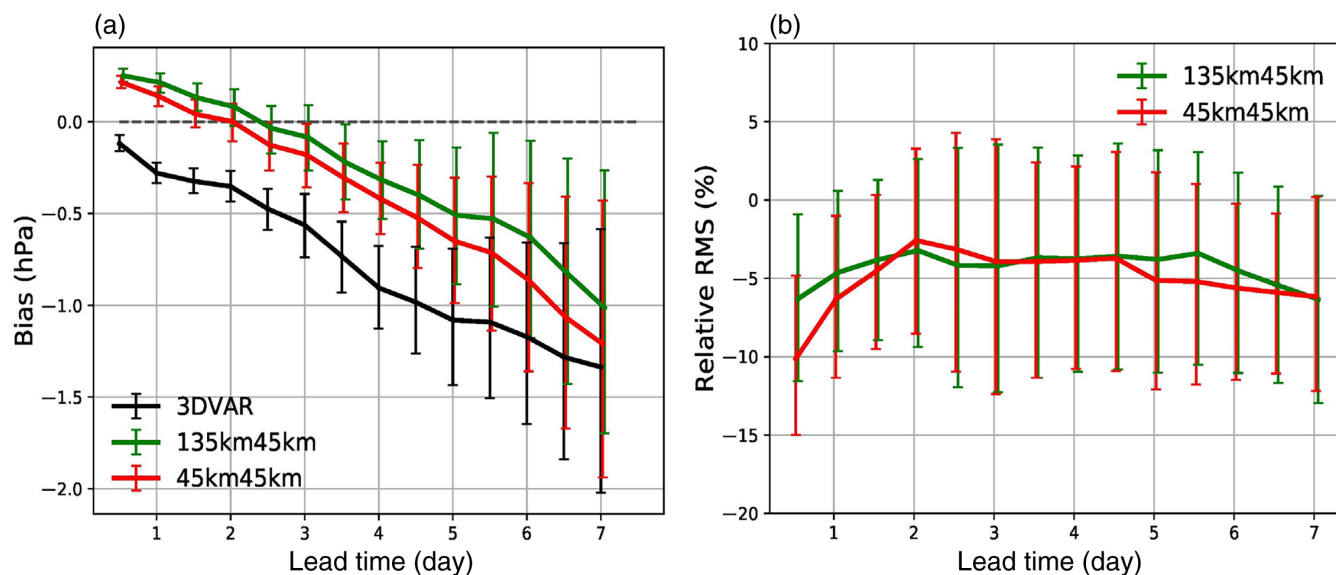


FIGURE 7 (a) Bias (hPa) of surface pressure forecasts from three experiments with respect to the Global Forecast System analysis as a function of forecast lead time. (b) Relative root mean square (RMS) (%) between the MRI-4DVAR experiments and 3DVAR. The vertical bars show 95% confidence interval after 8,000 bootstrap resamplings. [Colour figure can be viewed at wileyonlinelibrary.com]

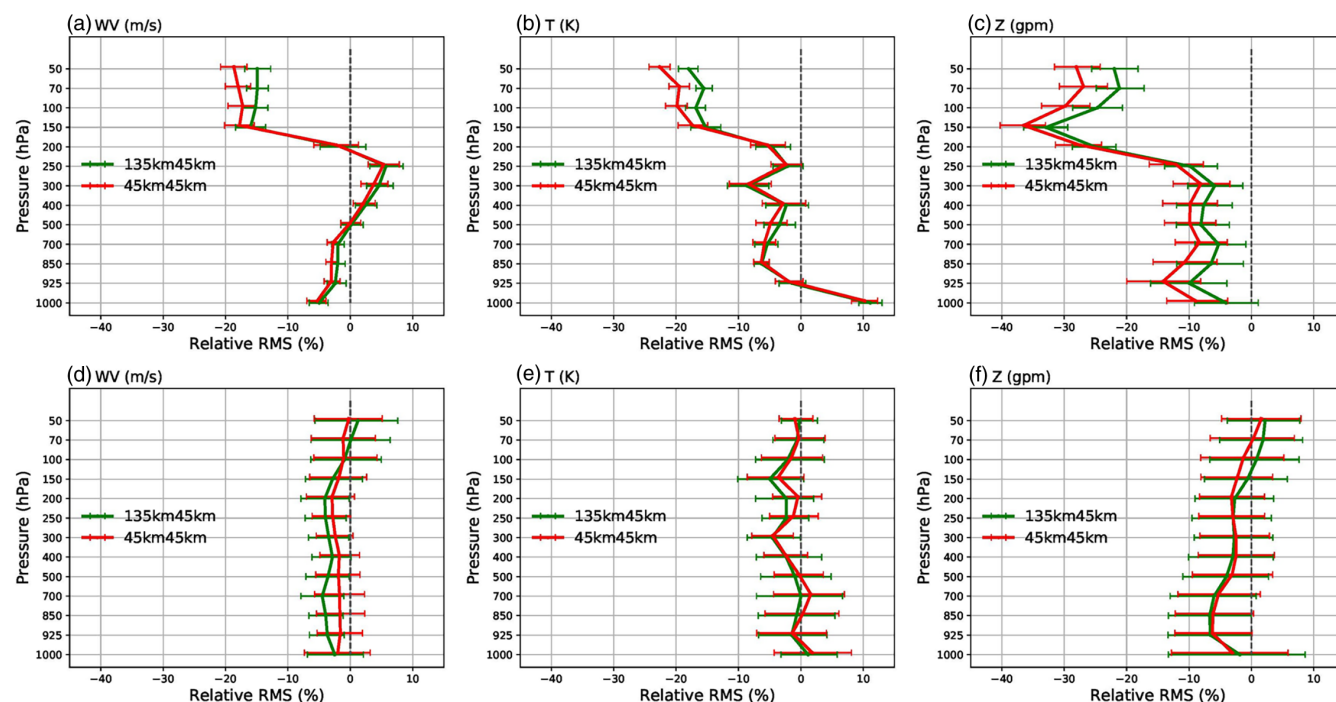


FIGURE 8 The relative root mean square (RMS) (%) between the MRI-4DVAR experiments and 3DVAR versus Global Forecast System analyses for 12-hr (top) and seven-day (bottom) forecasts of wind vector (WV), temperature, and geopotential height. The horizontal bars show 95% confidence intervals after 8,000 bootstrap resamplings. [Colour figure can be viewed at wileyonlinelibrary.com]

the three experiments, by comparing to the GFS analysis, observations from two drifting buoys, and cloud pattern from composite satellite imagery.

Figure 9 shows the sea level pressure (SLP) forecast initialized at 0000 UTC 11 August from the three experiments compared with the GFS analysis. On 12 August, the

central pressure of AC3 over the Laptev Sea reached about 986 hPa and SLP from the three runs are almost overlaid with the GFS analysis. On 14 August, there are two strong cyclone centers in the GFS analysis, one is AC1 over the Kara Sea with a central pressure of 985 hPa and the other is AC2 over the Arctic Ocean with 991 hPa. MRI-4DVAR

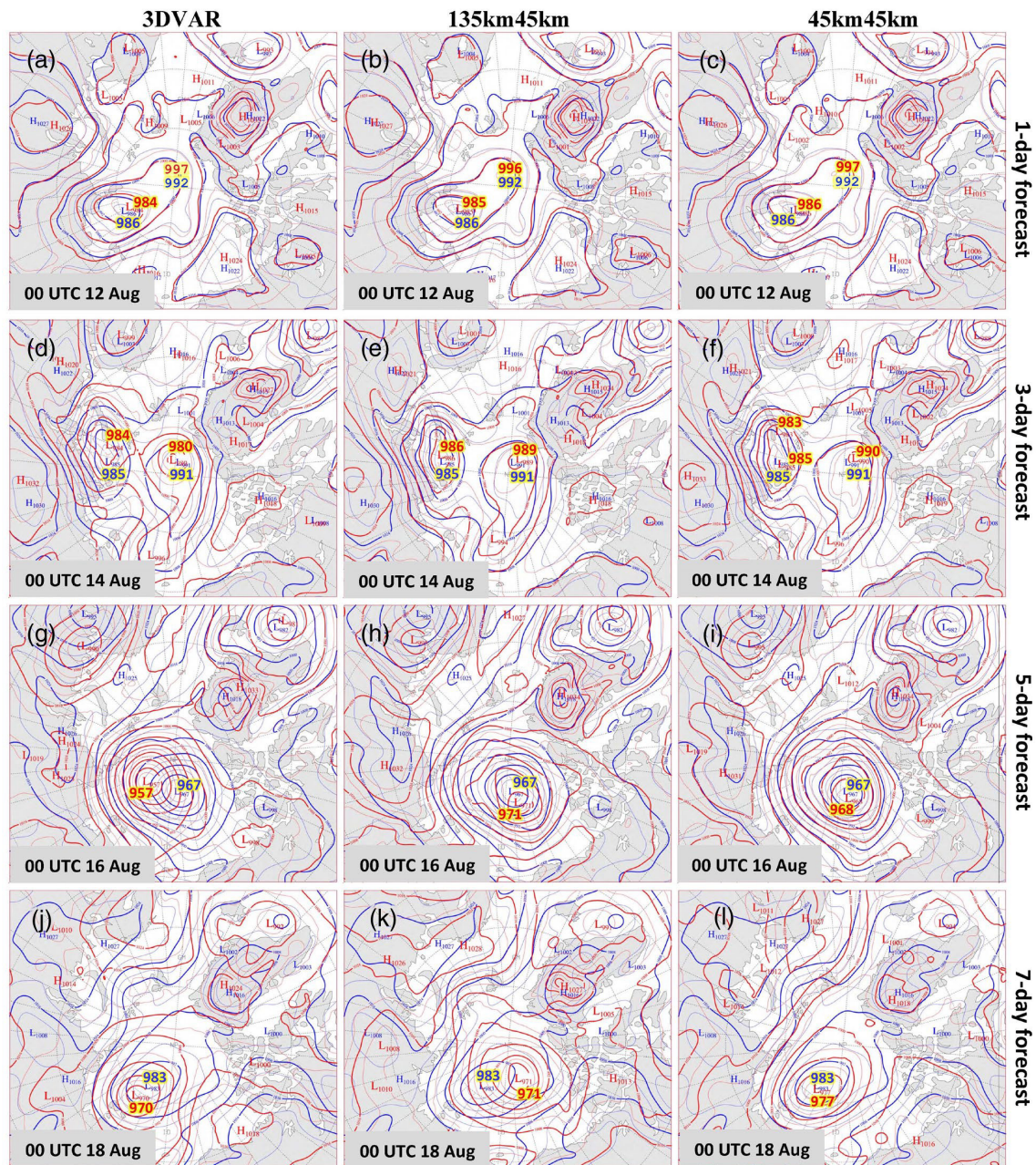


FIGURE 9 Sea level pressure of the Global Forecast System analysis (blue) overlaid with the corresponding Weather Research and Forecasting (WRF) day-1/3/5/7 forecast (red) from 3DVAR (left column), 135km45km MRI-4DVAR (middle column), and 45km45km MRI-4DVAR (right column). Valid times of analyses/forecasts are marked in each panel. Contour interval is 4 hPa. [Colour figure can be viewed at wileyonlinelibrary.com]

captured both cyclone centers with better location and intensity than 3DVAR. On 16 August, the GFS analysis shows AC16 covering the entire Pacific sector of the Arctic Ocean with 967 hPa central pressure. The cyclone central SLP from 45km45km is 1 hPa higher than in the GFS analysis and almost overlaid with it. The cyclone center from 3DVAR is about 600 km to the west of the center in the GFS analysis with a 10 hPa lower SLP. The prediction from 135km45km is slightly degraded in comparison to that of 45km45km. On 18 August, while both 3DVAR and

135km45km have a large displacement of the cyclone center, 45km45km (977 hPa) is still in very good agreement with the GFS analysis (983 hPa) in terms of the center location though with a 6 hPa lower central SLP. The pressure field surrounding the Arctic Ocean suffers from errors in the GFS forecast propagating through the lateral boundary, but as will be seen below these do not impact the forecast of AC16 that is centered over the Arctic Ocean.

Figure 10 shows SLP from the GFS forecasts and those from 45km45km overlaid with the GFS analysis.

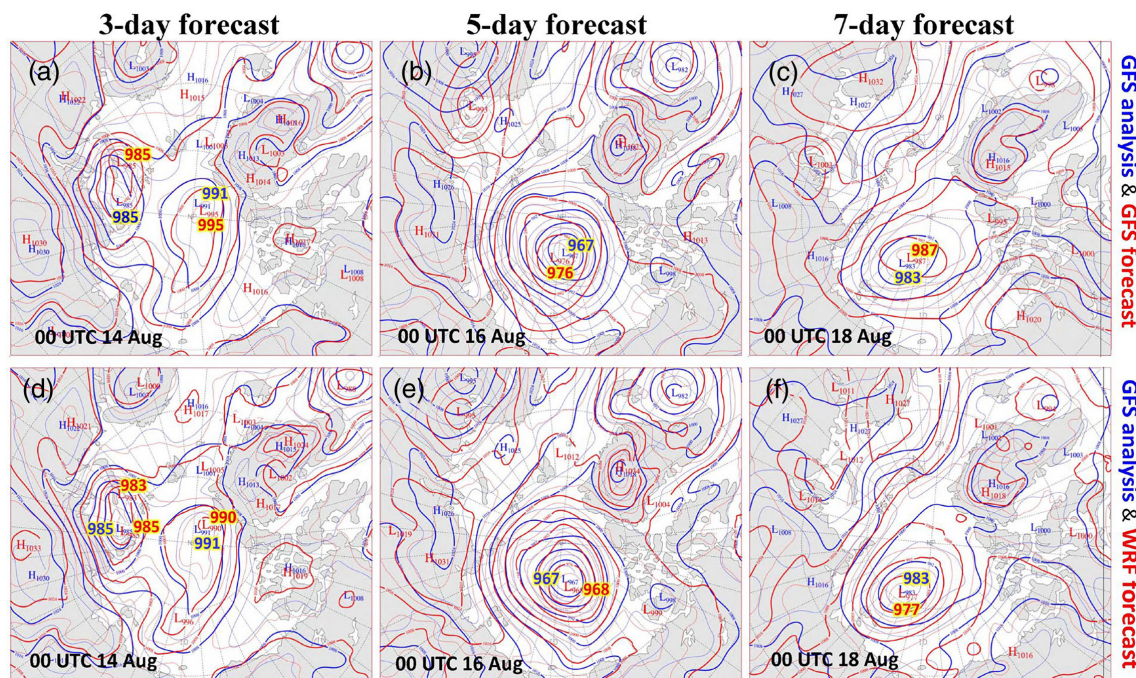


FIGURE 10 Sea level pressure of the Global Forecast System (GFS) analysis (blue) overlaid with the GFS day-3/5/7 forecast (red) (upper panels) and with Weather Research and Forecasting (WRF) forecast (red) from the 45km45km MRI-4DVAR experiment (lower panels). Contour interval is 4 hPa. [Colour figure can be viewed at wileyonlinelibrary.com]

For the three-day forecast from GFS and 45km45km (Figure 10a,d), the position and amplitude of ACs are comparable even though there is a small position shift in GFS and 45km45km compared with the GFS analysis. For AC1, the center location from 45km45km is just next to the location from GFS analysis, although there is a second center close to Novaya Zemlya which is caused by the topography, while the center location from the GFS forecast shifted westward over Novaya Zemlya. The SLP of AC16 in the GFS five-day forecast is about 976 hPa, while that in 45km45km is about 968 hPa and much closer to 967 hPa in the GFS analysis. Location error of the GFS seven-day forecast (Figure 10f) is larger than that of 45km45km. This forecast result demonstrates that regional prediction using Polar WRF initialized by MRI-4DVAR has significantly improved on the skill of the GFS forecasts that provide the lateral boundary conditions for the Polar WRF forecasts. Because Yamagami *et al.* (2018a) included this case in their sample and concluded that forecasting cyclones over the central Arctic is less skillful for longer than five days, this encouraging result indicates the potential for skillful regional AC forecasts beyond five days.

Over the Arctic Ocean, in situ meteorological observations are sparsely distributed and drifting buoys are a good data source providing surface data in the sea-ice-covered regions. According to Yamagami *et al.* (2017), the radius and center of AC16 were about 1,028 km and 187.60° E,

84.56° N respectively. We chose two drifting buoys, buoy ID 48510 (hereafter, buoy48510) and buoy ID 25623 (hereafter, buoy25623), to verify the three runs. One is on the north side of AC16 and the other is on the west side. The tracks of the two drifting buoys and the center of AC16 are marked in Figure 11a.

Figure 11b shows mean and RMS errors of day-1 to day-7 forecasts verified against P_s observations from the two buoys. The P_s forecasts from the three runs are higher than the observations. The mean of F–O (Forecast minus Observation) between 3DVAR and buoy25623 was as high as 3.5 hPa, while for 135km45km (45km45km) the mean is reduced to 0.2 hPa (0.3 hPa). Verified against buoy48510, the mean from 3DVAR is the smallest among three runs, although it is due to the large variation in the sign of F–O between relatively large positive and negative values (Figure 11e). Compared with 3DVAR, the averaged RMS error from 135km45km (45km45km) decreases 21.9% (64.1%) for buoy48510 and decreases 30.3% (72.7%) for buoy25623.

Figure 11c,d shows time series of P_s from the two drifting buoys from 11 to 18 August 2016. For both buoys, there are two main drops of P_s (around 13 and 16 August, days 2 and 5) during the period. Around 13 August, the P_s from both buoys dropped about 10 hPa in 24 hours. According to Section 2 and Yamagami *et al.* (2017), AC3 merged with AC2 on 13 August, so the observed P_s drop from the two buoys is related to the cyclone merger. During 14–16

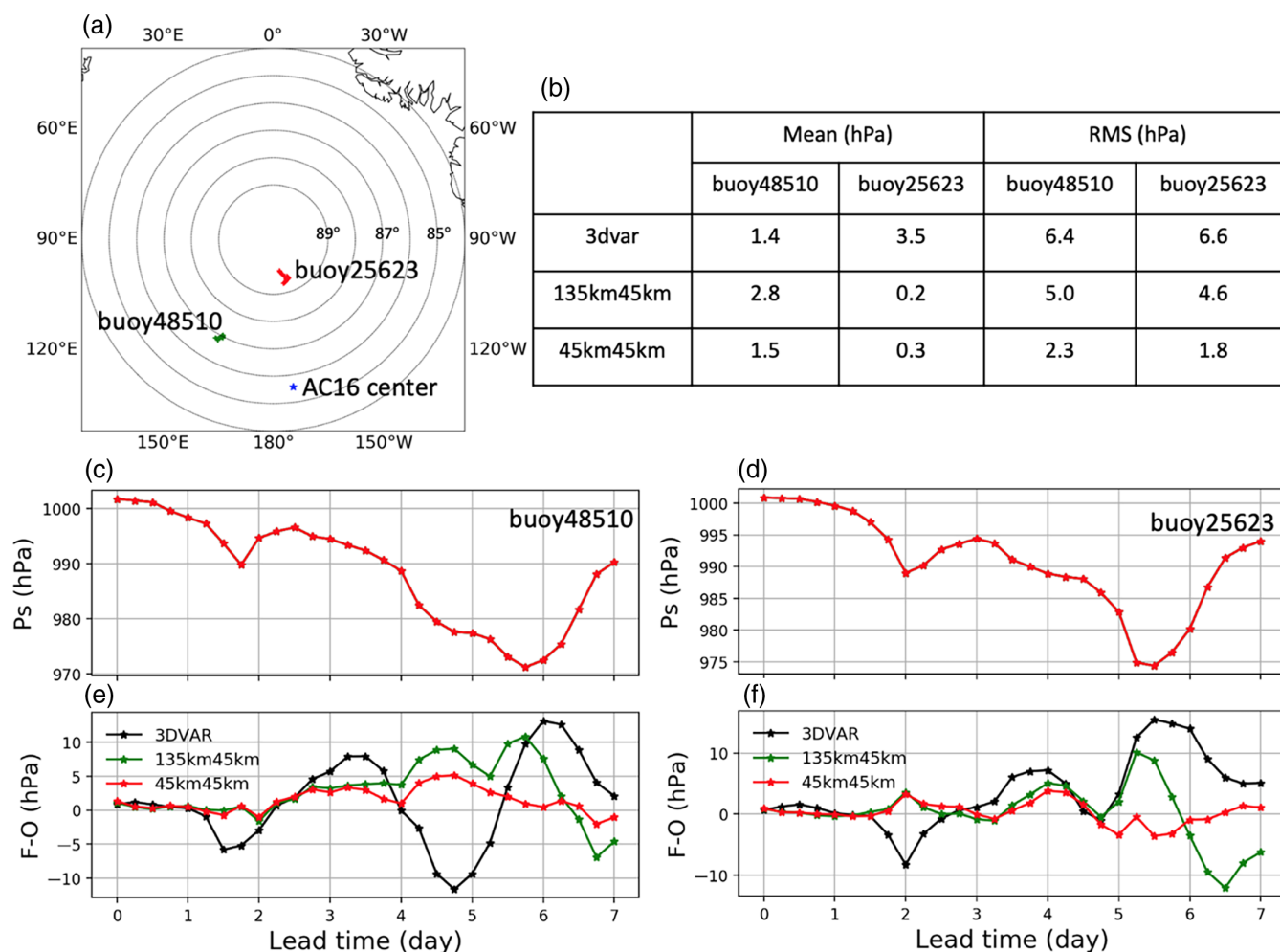


FIGURE 11 (a) Tracks of two drifting buoys from 11 to 18 August 2016 and the AC16 center at 0000 UTC on 16 August. (b) Mean and root mean square (RMS) errors of day-1 to day-7 forecast verified against the two buoys. (c, d) Time series of observed surface pressure from the two buoys from 0000 UTC 11 August (day 0) to 0000 UTC 18 August (day 7) 2016. (e, f) Forecast minus Observation (F–O) as a function of forecast lead time for the three experiments. [Colour figure can be viewed at wileyonlinelibrary.com]

August, the P_s from two buoys dropped continuously and reached the lowest P_s at 1800 UTC and 1200 UTC 16 August, respectively, due to AC16, which is consistent with Figure 1f.

Figure 11e,f depicts F–O as a function of forecast lead time from the three experiments. At 1800 UTC 12 August (0000 UTC 13 August) for buoy48510 (buoy25623) (during the cyclone merge), P_s from the two MRI-4DVAR experiments are very close to the two buoys (Figure 11e,f), whereas P_s from 3DVAR is lower than the observations by over 5 hPa (9 hPa) respectively. For buoy25623, which was close to the AC16 center, the deep P_s from 3DVAR (Figure 11f) on 13 August is consistent with results from previous discussion in Figure 9. The maximum F–O from 3DVAR is over 10 hPa around 16 August compared to the two buoys. In contrast, the 45km45km experiment exhibited stable F–O with only a small variation of the F–O value over the seven-day forecasts. Overall 135km45km's

performance is between 3DVAR and 45km45km, and for the first five days the 135km45km results are close to those of 45km45km.

To illustrate the forecast performance for clouds, we compare outgoing longwave radiation (OLR) at the top of the atmosphere (TOA) with the satellite composite imagery retrieved from the Antarctic Meteorological Research Center (AMRC) archive at the University of Wisconsin–Madison (Kohrs *et al.*, 2014). The OLR image used here was downloaded from ftp://amrc.ssec.wisc.edu/archive/ and at a 4-km grid spacing. Figure 12 shows the five-day forecast TOA OLR from the three experiments and composite satellite imagery. SLP from the GFS analysis (Figure 12a) and from the day-5 forecast of the three experiments (Figure 12b–d) are also overlaid with the OLR images to better identify the cyclone center and surrounding cloud features. Compared to the composite satellite image, the five-day forecast OLR patterns from two

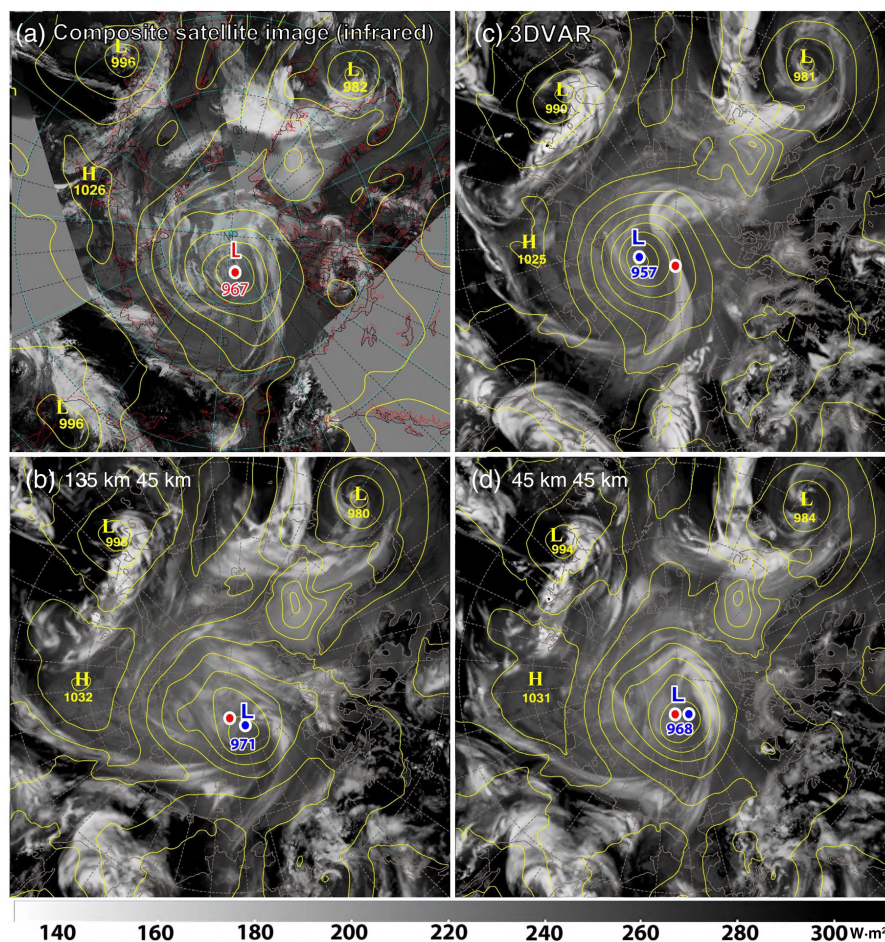


FIGURE 12 (a) Composite satellite imagery overlaid with Global Forecast System (GFS) sea level pressure (SLP) analysis, and Polar Weather Research and Forecasting (WRF) day-5 forecast of top of atmosphere outgoing longwave radiation (OLR, $\text{W} \cdot \text{m}^{-2}$) overlaid with SLP from (b) 3DVAR, (c) 135km45km, and (d) 45km45km, valid at 0000 UTC 16 August 2016. Red-filled circles with white outline show the location of the cyclone center from the GFS analysis, and the blue-filled circles locate the forecast centers. Contour interval is 8 hPa. [Colour figure can be viewed at wileyonlinelibrary.com]

MRI-4DVAR runs have a better agreement than 3DVAR with the observed cloud patterns around the extreme Arctic cyclone center, especially for the frontal cloud band to the right of the center in 45km45km.

The significantly improved forecast skill of AC16 up to and beyond five days from MRI-4DVAR is encouraging and we explore the reasons for the improvement in the following subsection by analyzing the structure of the dynamic and thermodynamic fields and their evolution.

4.3.2 | Upper-level forecasts and the impact of initial conditions on AC16

In this subsection, we analyze the forecast of AC16 from the view of dynamic and thermodynamic mechanisms and investigate the impact of initial conditions on the prediction of this storm. Because the two MRI-4DVAR figures are similar (especially at the initial time), the results of 135km45km MRI-4DVAR are not presented here. We use “4DVAR” to represent “45km45km MRI-4DVAR”.

Baroclinic instability is the major mechanism of cyclone genesis and development, and is often used to interpret formation, intensification, and persistence of

Arctic cyclones (e.g., Yanase and Niino, 2007; Yamagami *et al.*, 2017; Yamagami *et al.*, 2018a, 2018b; Akperov *et al.*, 2020). The maximum Eady growth rate (EGR) is a measure of baroclinic instability (Eady, 1949); it indicates how conducive the environment is to cyclogenesis and deepening (e.g., Hoskins and Valdes, 1990; Pierrehumbert and Swanson, 1995). EGR is defined using the vertical wind shear and the Brunt–Väisälä frequency:

$$\text{EGR} = 0.3098 \frac{f \left| \frac{\partial U}{\partial z} \right|}{N}, \quad (1)$$

$$N^2 = \frac{g}{\theta} \frac{\partial \theta}{\partial z}, \quad (2)$$

where f is the Coriolis parameter, $\partial U / \partial z$ is the vertical wind shear, U is the horizontal wind vector, and z is the vertical coordinate. Due to the thermal wind balance, the vertical wind shear is connected to the horizontal temperature gradient. N is the Brunt–Väisälä frequency, which depends on the vertical gradient of the potential temperature where g is the gravity acceleration and θ is the potential temperature. EGR is calculated at 400 hPa, that is below the strongest wind speeds and

where the horizontal temperature gradients contribute to vertical wind shear. *EGR* is used to investigate the baroclinic instability that is connected with the upper-level jet stream.

Forecast results initialized by 3DVAR and 4DVAR data assimilation experiments

The synoptic analysis in Section 2 showed that multiple processes contributed to the evolution of AC16. For the comparison of forecast results initialized by 3DVAR and 4DVAR, the impacts of baroclinicity, polar vortex, jet stream and TPVs on the storm development are investigated according to the stages described in Section 2.

Initial stage. From 11 to 13 August, the cyclonic circulation of AC1 in 3DVAR (Figure 13b) develops slower than in 4DVAR (Figure 13e), facilitating greater subsequent intensification. In the forecast initialized by 3DVAR, the upper-level jet streak (adjacent to TPV1 and PV) becomes stronger than 4DVAR (Figure 14a,d). The polar vortex PV was overintensified in 3DVAR after TPV4 and TPV3 merged into PV from 11 to 13 August (Figures 1b and 13b,e) because of the stronger TPV4 and TPV3 (not shown). The overdeveloped PV in 3DVAR (Figure 15a,b) enhanced AC2 by 13 August (980 hPa compared with 986 hPa in 4DVAR [Figure 13b,e]).

Early development stage. From 13 to 14 August, the fronts of AC1 were starting to occlude in 4DVAR while in 3DVAR they were actively developing (Figure 13c,f). AC2 fully coupled with the polar vortex PV in 3DVAR with an axisymmetric vertical structure and the central location was shifted compared to 4DVAR (Figures 13c,f and 15b,e). The deeper polar vortex PV in 3DVAR increased the thermal gradient between PV and the jet especially along the colder trough to the south of the PV center (Figure 14b,e). According to the thermal wind balance, the stronger temperature gradient intensified the jet stream as reflected by the *EGR* (Figure A1c,f); the developing cyclone AC1 was supported by the right entrance of the dominant jet streak (Figure 14c,f). The enhanced PV extended cyclonic flow from the tropopause to low levels which helped to intensify AC2 (980 hPa in 3DVAR and 990 hPa in 4DVAR; Figure 13c,f). The deeper polar vortex, earlier coupling between the low-level cyclone and the polar vortex PV, and stronger jet stream led to the earlier development of AC2 in 3DVAR.

Rapid intensification stage. From 14 to 15 August, the central pressure of AC1 in 3DVAR dropped 24 hPa from

984 to 960 hPa (from 985 to 973 hPa in 4DVAR) during the merger of AC1 with AC2 and TPV1 with the polar vortex PV (Figure 13c,f,g,j). TPV1 was intensified and deeper in 3DVAR than 4DVAR and coupled with the low-level cyclone AC1 (not shown). PV in 3DVAR started to intensify when being coupled with the intensified surface low system AC2 because of earlier coupling on 0000 UTC 14 August (Figure 13g,j). For 3DVAR, the amplified baroclinic instability at the jetstream level shown by *EGR* (Figure A1c,f,g,j), the stronger upper jet stream (close to TPV1) (Figure 14b,e), and intensified vortices (TPV1 and the polar vortex PV) led to the stronger and faster baroclinic development of cyclone system AC1 (0000 UTC 14 August to 0000 UTC 15 August).

Later development stage. From 15 to 16 August, the predicted central pressure of AC16 based on 3DVAR initialization dropped to 957 hPa and was 11 hPa lower than 4DVAR (968 hPa). In the 3DVAR forecast, TPV1 fully merged into PV (Figures 14c and 15c) and AC16 vertically coupled with PV16 (previously PV), which led to the stronger surface cyclone (AC16). In the forecast initialized by 4DVAR, TPV1 did not fully merge with PV16 and they are displaced from each other (Figures 14f and 15f).

Dissipating stage. After 16 August, AC16 began to dissipate and linger over the Arctic Ocean for several days. AC16 and PV16 became a barotropic system, and the low-level cyclone was coupled with the upper-level polar vortex. The predicted central pressure of AC16 based on 3DVAR initialization was 963 hPa and still lower than 4DVAR (971 hPa). The centers of surface low and polar vortex were fully overlaid in 3DVAR with strong vertical coupling and in 4DVAR the low-level pressure center was still displaced from the upper-level vortex (Figure 13i,l). The 3DVAR complete vertical coupling and barotropic structure are similar to the long-lasting storm studied by Tao *et al.* (2017b). The polar vortex steered the cyclonic circulation of the whole system from tropopause to surface while keeping the storm over the Arctic Ocean.

The impact of initial conditions on the forecast of AC16

Based on the synoptic and forecast analysis of the AC16 case study, the impacts of initial conditions from 3DVAR and 4DVAR at 0000 UTC 11 August on the forecast performance are investigated by analyzing the dynamic and thermodynamic structure and differences between them. In the initial condition from 3DVAR compared to 4DVAR, TPV4 and TPV3 as well as the jet streams and

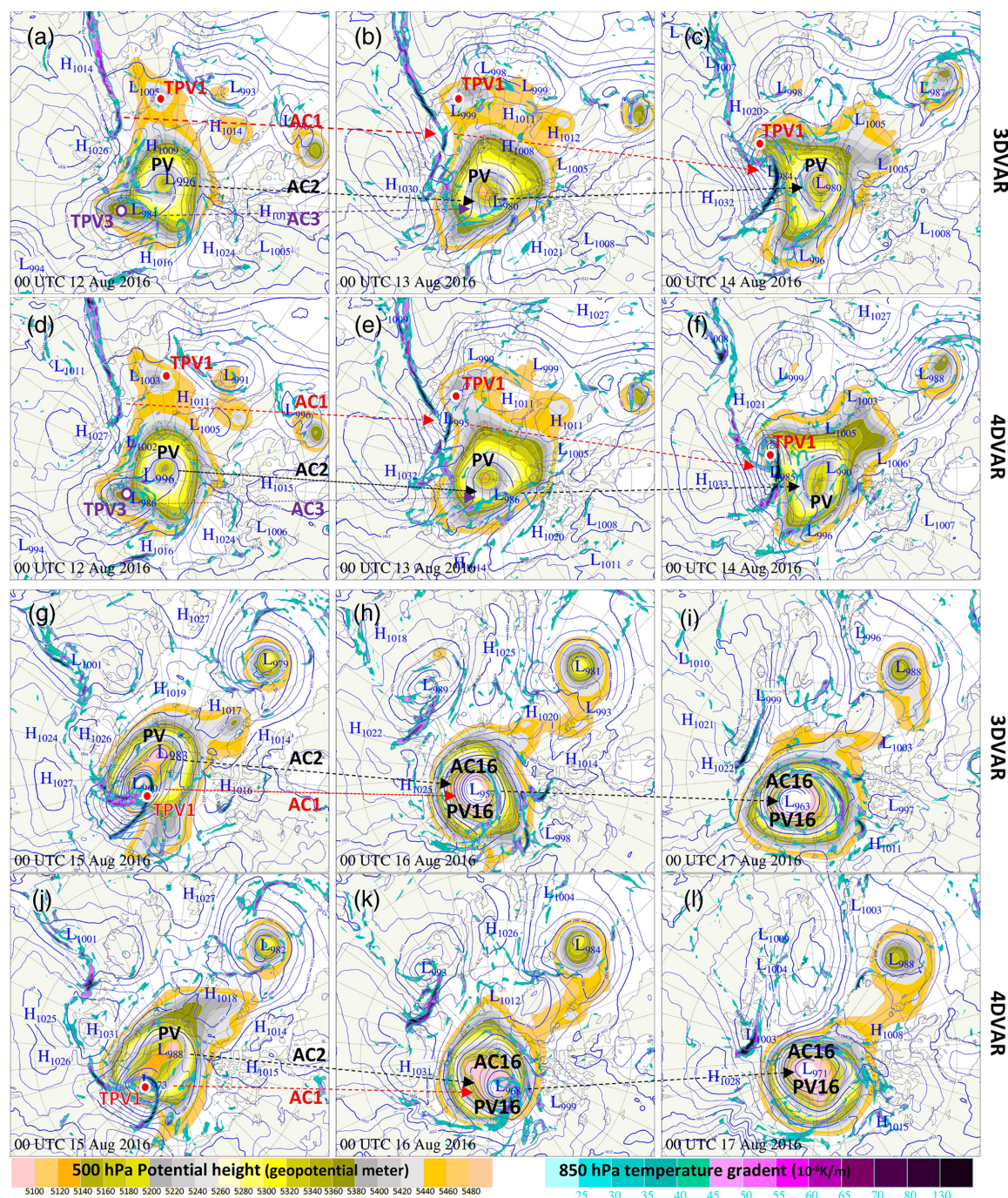


FIGURE 13 Temperature gradient at 850 hPa (shaded), sea level pressure (SLP) (contour interval is 4 hPa in blue), and 500-hPa geopotential height (contour interval is 20 m shaded) from Weather Research and Forecasting (WRF) forecast initialized by 3DVAR and 4DVAR for 0000 UTC 12 August to 0000 UTC 17 August 2016. Tropopause Polar Vortex-1 (TPV1) (●) and TPV3 (○) show the high-level locations of TPVs. [Colour figure can be viewed at wileyonlinelibrary.com]

baroclinicity related to them via the *EGR* were amplified (Figure 16b,c,e,f). As a result of the enhanced TPV4 and TPV3 merging into the polar vortex PV, it was overintensified by 3DVAR from 11 to 13 August (Figure 13b,e). The stronger frontal zone at 850 hPa (Figure 16a,d), and the stronger jet stream on the 2-PVU surface (Figure 16b,e) can be seen near AC1 and TPV1, respectively. This shows

that AC1 was connected to stronger baroclinic systems and processes, which led to AC1's early baroclinic development in 3DVAR compared to 4DVAR. Similar to Tao *et al.*'s (2017a) analysis for AC12, TPVs (and the polar vortex PV) are associated with warm anomalies in the lower stratosphere that intensified the upper-level jet and the storm.

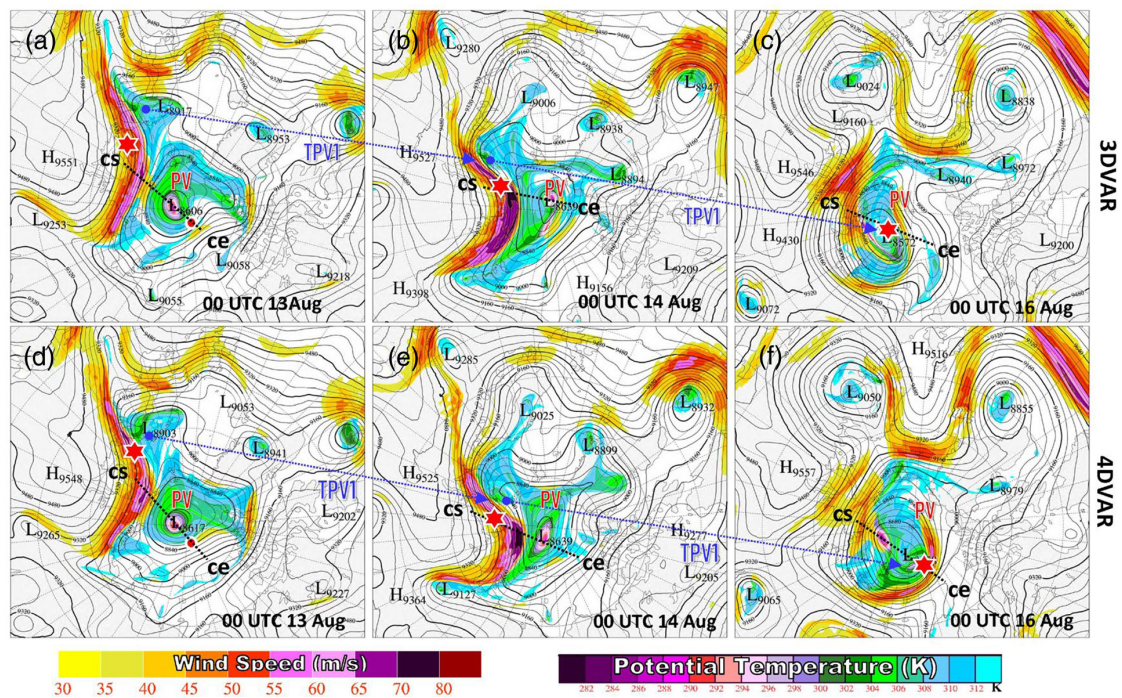


FIGURE 14 3DVAR and 4DVAR's day-2/3/5 forecast of 300-hPa geopotential height (contour interval is 40 m in black) overlaid with potential temperature (K, shaded) and wind speed ($\text{m}\cdot\text{s}^{-1}$, shaded) on the 2-potential vorticity unit surface. The dashed lines indicate the cross-sections from CS to CE in Figure 15. The blue arrow dashed lines show the track of Tropopause Polar Vortex-1 (TPV1). Valid times are marked in each panel. The symbols show the center location of cyclones AC1 (★) and AC3 (●). [Colour figure can be viewed at wileyonlinelibrary.com]

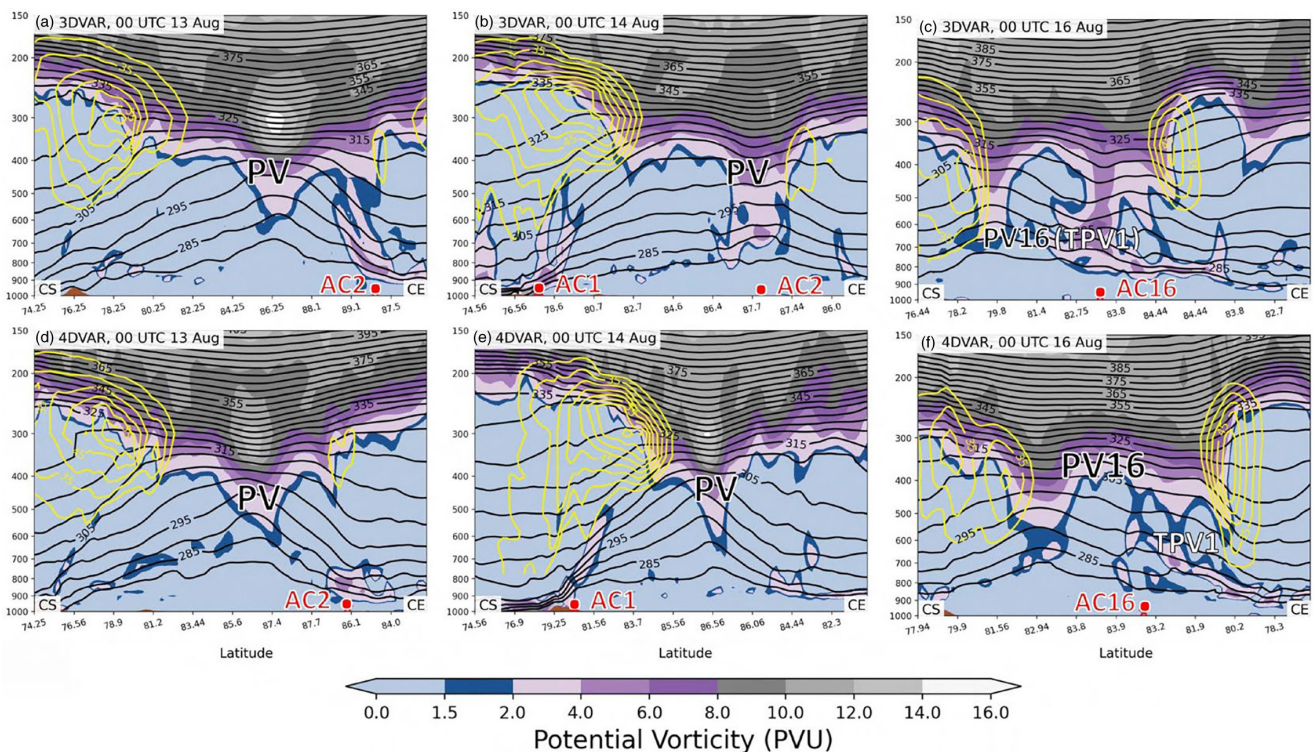


FIGURE 15 Cross-sections of potential vorticity (PVU, shaded), potential temperature (K; contour interval is 5 K in black) and wind speed ($\text{m}\cdot\text{s}^{-1}$; contour interval is 5 $\text{m}\cdot\text{s}^{-1}$ in yellow and the range is from 30 to 70 $\text{m}\cdot\text{s}^{-1}$) from day-2, day-3, and day-5 forecasts of the 3DVAR and 4DVAR. Cyclone center is marked by a red dot if the cross-section passes through the cyclone center. Terrain is in brown. Cross-sections are along the dashed lines from CS to CE in Figure 14. [Colour figure can be viewed at wileyonlinelibrary.com]

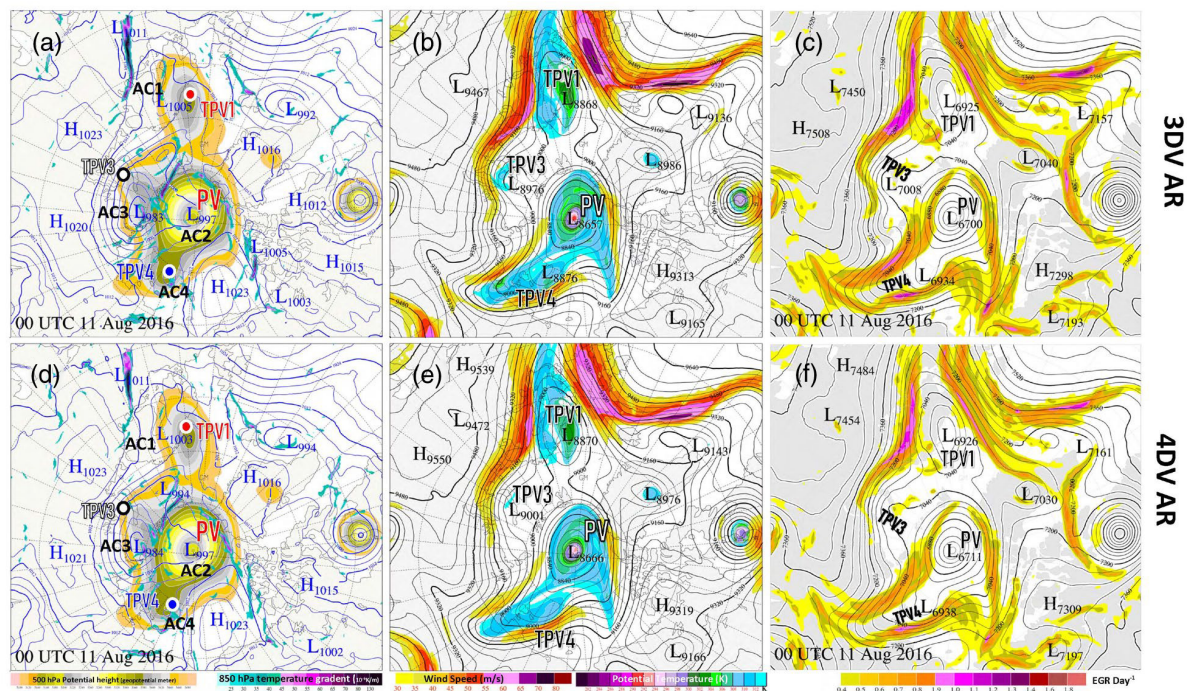


FIGURE 16 Analysis of 3DVAR and 4DVAR at 0000 UTC 11 August 2016. (a, d), 850-hPa temperature gradient (shaded), sea level pressure (contour interval is 4 hPa in blue), and 500-hPa geopotential height (contour interval is 20 m, shaded). (b, e), 300-hPa geopotential height (contour interval is 40 geopotential meters, black) overlaid with potential temperature (K, shaded) and wind speed ($\text{m}\cdot\text{s}^{-1}$, shaded) on the 2-potential vorticity unit surface. (c, f), 400-hPa geopotential height (black, contour interval is 40 geopotential meters) and Eady growth rate (EGR) (shaded, day^{-1} , between 450 hPa and 350 hPa). Tropopause Polar Vortex-1 (TPV1; ●), TPV3 (○) and TPV4 (●) in (a,d) show the high-level locations of TPVs in (b,e). [Colour figure can be viewed at wileyonlinelibrary.com]

Compared to the initial condition produced by 4DVAR, 3DVAR produced deeper polar vortex/TPVs, amplified baroclinic instability, intensified upper-level jet streams and a stronger frontal zone. These factors led to the displacement of center location and the much deeper central pressure in Polar WRF forecast of AC16 initialized by 3DVAR. For 4DVAR, the successful prediction of AC16 was due to the more accurate simulation of upper-level atmospheric fields, as shown for the 20-day cycling diagnostics (Figure 6) from Section 4.2. The better radiance assimilation in 4DVAR (see 11 August in Figure 6) contributed to the improvements in the upper-level fields. The better forecast results initialized by 4DVAR benefited from using the forecast model as a constraint to impose thermodynamic and dynamic balances (between the baroclinic processes, polar vortex/TPVs, and upper-level jet stream) on the data assimilation.

5 | CONCLUSIONS

In this study, the Polar WRF model and WRFDA (3DVAR and MRI-4DVAR) are applied to perform cycling data assimilations and forecast experiments for Arctic cyclone prediction to evaluate MRI-4DVAR performance during

a 20-day cycling run, and to investigate the impacts of initial conditions on the forecast skill of AC16 and identify the factors impacting its predictability. Importantly to mimic the forecast process, lateral boundary conditions for Polar WRF forecasts were taken from the GFS operational deterministic forecasts.

Statistical measures of averaged forecast performance over a 20-day cycling period indicate a clear benefit of MRI-4DAR when compared to 3DVAR, especially for lead times beyond five days with an about 6% RMS error reduction for day-7 SLP forecast. Compared to the 3DVAR experiment, using the recently developed multiresolution incremental 4DVAR (MRI-4DVAR) technique (Liu *et al.*, 2020) leads to a substantial forecast improvement of the extreme Arctic cyclone event that occurred on 16 August 2016 (AC16) while keeping its computational cost reasonable for real-time applications. A skillful SLP forecast of 5–7 days is obtained in terms of location and intensity of the extreme AC16 with a Polar WRF forecast grid spacing at 15 km and both MRI-4DVAR inner loop minimizations at 45 km.

Dynamic and thermodynamic (development) mechanisms are investigated for the AC16 case. The prediction of AC16 is challenging because it includes multiple processes, such as merging of Arctic cyclones,

merging of polar vortex/TPVs, baroclinic processes and vertical motions associated with jet streams. In the 3DVAR-generated initial conditions, the deeper TPV3 together with a stronger jet stream intensified AC2 during first two mergers on 12 and 13 August. Consequently, there was an earlier coupling between Arctic cyclone AC2 and the polar vortex PV on 14 August in the forecasts from 3DVAR. The deeper PV, earlier coupling between AC2 and PV, and stronger jet stream led to the earlier development of AC2 in 3DVAR. AC1 and TPV1, which merged into AC2 and PV on 16 August, also played an important role. The baroclinic instability adjacent to TPV1 was stronger in 3DVAR than in 4DVAR and was accompanied by a stronger jet stream that led to the overdevelopment of AC16 in 3DVAR. Yamagami *et al.* (2018b) mentioned that accurate prediction of upper-level fields is important for the prediction of ACs. For MRI-4DVAR, the successful prediction of AC16 is likely due to the more accurate simulation of upper-level atmospheric fields, which was facilitated by improved satellite radiance assimilation. The better forecast results initialized by 4DVAR benefited from using the forecast model as a constraint to impose thermodynamic and dynamic balances (between the baroclinic processes, polar vortex/TPVs, and upper-level jet stream) on the data assimilation. The better forecast skill for AC16 obtained here compared to the GFS deterministic model is a probable consequence of using a regional model and 4DVAR system optimized for Arctic conditions. The prominent role of the quasi-stationary polar vortex in the development of AC16 likely facilitated the success of these medium-range forecasts.

This study assimilated conventional observations and temperature-sensitive AMSU-A radiances from four satellites. Further improvement could potentially be made by assimilating more satellite radiance data in MRI-4DVAR, such as from the humidity-sensitive Microwave Humidity Sounder (MHS) and Infrared Atmospheric Sounding Interferometer (IASI). The assimilation of MHS and IASI data will substantially increase the amount of satellite radiances as well as better depicting the atmosphere's humidity structure. WRF MRI-4DVAR has been successfully applied to improve severe-storm prediction at convective scale (Liu *et al.*, 2020; Wu *et al.*, 2020), and we plan to apply it to ACs from other years to confirm the generality of the forecast improvement shown here.

AUTHOR CONTRIBUTIONS

Junmei Ban: Conceptualization; data curation; formal analysis; software; validation; visualization; writing – original draft. **Zhiquan Liu:** Conceptualization; formal analysis; funding acquisition; investigation; methodology; project administration; supervision;

validation; writing – original draft. **David H. Bromwich:** Conceptualization; formal analysis; funding acquisition; investigation; methodology; project administration; supervision; validation; writing – original draft. **Lesheng Bai:** Data curation; formal analysis; investigation; methodology; software; validation; visualization; writing – original draft.

ACKNOWLEDGEMENTS

The work is supported by the ONR grants N00014-18-1-2361 and N00014-21-1-2650. NCAR is sponsored by the National Science Foundation. Contribution 1605 of Byrd Polar and Climate Research Center. Thanks to the three anonymous reviewers for their insightful comments.

DATA AVAILABILITY STATEMENT

The numerical model output that is the basis for this analysis amounts to more than 10 TB and is archived at the Ohio Supercomputer Center. Contact David Bromwich (bromwich.1@osu.edu) to obtain access to these voluminous data sets.

ORCID

Zhiquan Liu  <https://orcid.org/0000-0003-4917-7686>

David H. Bromwich  <https://orcid.org/0000-0003-4608-8071>

REFERENCES

- Akperov, M., Semenov, V., Mokhov, I., Dorn, W. and Rinke, A. (2020) Impact of Atlantic water inflow on winter cyclone activity in the Barents Sea: insights from coupled regional climate model simulations. *Environmental Research Letters*, 15, 024009. <https://doi.org/10.1088/1748-9326/ab6399>.
- Auligné, T., McNally, A.P. and Dee, D.P. (2007) Adaptive bias correction for satellite data in a numerical weather prediction system. *Quarterly Journal of the Royal Meteorological Society*, 133, 631–642.
- Barker, D., Huang, X.Y., Liu, Z., Auligné, T., Zhang, X., Rugg, S., Ajjaji, R., Bourgeois, A., Bray, J., Chen, Y. and Demirtas, M. (2012) The weather research and forecasting model's community variational/ensemble data assimilation system: WRFDA. *Bulletin of the American Meteorological Society*, 93, 831–843. <https://doi.org/10.1175/BAMS-D-11-00167.1>.
- Bromwich, D.H., Hines, K.M. and Bai, L.-S. (2009) Development and testing of polar weather research and forecasting model: 2. Arctic Ocean. *Journal of Geophysical Research*, 114, D08122. <https://doi.org/10.1029/2008JD010300>.
- Cavallo, S.M. and Hakim, G.J. (2009) Potential vorticity diagnosis of a tropopause polar cyclone. *Monthly Weather Review*, 137, 1358–1371. <https://doi.org/10.1175/2008MWR2670.1>.
- Cavallo, S.M. and Hakim, G.J. (2010) Composite structure of tropopause polar cyclones. *Monthly Weather Review*, 138, 3840–3857. <https://doi.org/10.1175/2010MWR3371.1>.
- Chen, F. and Dudhia, J. (2001) Coupling an advanced land-surface-hydrology model with the Penn State-NCAR

- MM5 modeling system. Part I: model description and implementation. *Monthly Weather Review*, 129, 569–585. [https://doi.org/10.1175/1520-0493\(2001\)129<0569:CAALSH>2.0.CO;2](https://doi.org/10.1175/1520-0493(2001)129<0569:CAALSH>2.0.CO;2).
- Courtier, P., Thépaut, J.-N. and Hollingsworth, A. (1994) A strategy for operational implementation of 4D-Var, using an incremental approach. *Quarterly Journal of the Royal Meteorological Society*, 120, 1367–1387.
- De Silva, L.W.A. and Yamaguchi, H. (2019) Grid size dependency of short-term sea ice forecast and its evaluation during extreme Arctic cyclone in August 2016. *Polar Science*, 21, 204–211.
- Eady, E.T. (1949) Long waves and cyclone waves. *Tellus*, 1, 33–52. <https://doi.org/10.1111/j.2153-3490.1949.tb01265.x>.
- Errico, R.M. (1997) What is an adjoint method? *Bulletin of the American Meteorological Society*, 78, 2577–2591.
- Errico, R.M. and Raeder, K.D. (1999) An examination of the accuracy of the linearization of a mesoscale model with moist physics. *Quarterly Journal of the Royal Meteorological Society*, 125, 169–195.
- Errico, R.M., Vukićević, T. and Raeder, K. (1993) Examination of the accuracy of a tangent linear model. *Tellus*, 45A, 462–477. <https://doi.org/10.1034/j.1600-0870.1993.00010.x>.
- Gauthier, P., Tanguay, M., Laroche, S., Pellerin, S. and Morneau, J. (2007) Extension of 3D-Var to 4D-Var: implementation of 4D-VAR at the meteorological service of Canada. *Monthly Weather Review*, 135, 2339–2354.
- Gauthier, P. and Thépaut, J.-N. (2001) Impact of the digital filter as a weak constraint in the preoperational 4DVAR assimilation system of Météo-France. *Monthly Weather Review*, 129, 2089–2102.
- Goodrum, G., Kidwell, K.B. and Winston, W. (1999) NOAA KLM User's Guide. National Oceanic and Atmospheric Administration, CD-ROM.
- Gray, S.L., Hodges, K.I., Vautrey, J.L. and Methven, J. (2021) The role of tropopause polar vortices in the intensification of summer Arctic cyclones. *Weather Climate Dynamics*, 2, 1303–1324. <https://doi.org/10.5194/wcd-2-1303-2021>.
- Hakim, G.J. (2000) Climatology of coherent structures on the extratropical tropopause. *Monthly Weather Review*, 128, 385–406. [https://doi.org/10.1175/15200493\(2000\)128<0385:COCSOT>2.0.CO;2](https://doi.org/10.1175/15200493(2000)128<0385:COCSOT>2.0.CO;2).
- Hakim, G.J. and Canavan, A.K. (2005) Observed cyclone-anticyclone tropopause vortex asymmetries. *Journal of the Atmospheric Sciences*, 62, 231–240. <https://doi.org/10.1175/JAS-3353.1>.
- Han, Y., van Delst, P., Liu, Q., Weng, F., Yan, B., Treadon, R. and Derber, J. (2006) *JCSDA Community Radiative Transfer Model (CRTM)—Version 1*, Vol. 122. Washington, DC: NOAA Tech. Rep. NESDIS, p. 40.
- Hines, K.M. and Bromwich, D.H. (2008) Development and testing of polar weather research and forecasting (WRF) model. Part I: Greenland ice sheet meteorology. *Monthly Weather Review*, 136, 1971–1989. <https://doi.org/10.1175/2007MWR2112.1>.
- Hines, K.M., Bromwich, D.H., Bai, L.-S., Barlage, M. and Slater, A.G. (2011) Development and testing of polar WRF. Part III: Arctic land. *Journal of Climate*, 24, 26–48. <https://doi.org/10.1175/2010JCLI3460.1>.
- Hines, K.M., Bromwich, D.H., Bai, L.-S., Bitz, C.M., Powers, J.G. and Manning, K.W. (2015) Sea ice enhancements to polar WRF. *Monthly Weather Review*, 143, 2363–2385. <https://doi.org/10.1175/MWR-D-14-00344.1>.
- Hoskins, B.J. and Valdes, P.J. (1990) On the existence of storm-tracks. *Journal of the Atmospheric Sciences*, 47, 1854–1864.
- Huang, X.-Y., Xiao, Q., Barker, D.M., Zhang, X., Michalakes, J., Huang, W., Henderson, T., Bray, J., Chen, Y., Ma, Z. and Dudhia, J. (2009) Four-dimensional variational data assimilation for WRF: formulation and preliminary results. *Monthly Weather Review*, 137, 299–314. <https://doi.org/10.1175/2008MWR2577.1>.
- Iacono, M.J., Delamere, J.S., Mlawer, E.J., Shephard, M.W., Clough, S.A. and Collins, W.D. (2008) Radiative forcing by long-lived greenhouse gases: calculations with the AER radiative transfer models. *Journal of Geophysical Research*, 113, D13103. <https://doi.org/10.1029/2008JD009944>.
- Inoue, J. (2021) Review of forecast skills for weather and sea ice in supporting Arctic navigation. *Polar Science*, 27, 100523. <https://doi.org/10.1016/j.polar.2020.100523>.
- Kadowaki, T. (2005) A 4-dimensional variational assimilation system for the JMA global spectrum model. *CAS/JSC WGNE Research Activities in Atmospheric and Oceanic Modelling*, 34, 117–118.
- Kain, J.S. (2004) The Kain–Fritsch convective parameterization: an update. *Journal of Applied Meteorology*, 43, 170–181.
- Kohrs, R.A., Lazzara, M.A., Robaidek, J.O., Santek, D.A. and Knuth, S.L. (2014) Global satellite composites—20 years of evolution. *Atmospheric Research*, 135, 8–34.
- Laroche, S., Gauthier, P., Tanguay, M., Pellerin, S. and Morneau, J. (2007) Impact of the different components of 4DVAR on the global forecast system of the meteorological service of Canada. *Monthly Weather Review*, 135, 2355–2364.
- Liu, Z., Ban, J., Hong, J.S. and Kuo, Y.-H. (2020) Multi-resolution incremental 4D-VAR for WRF: implementation and application at convective scale. *Quarterly Journal of the Royal Meteorological Society*, 146, 3661–3674.
- Liu, Z. and Rabier, F. (2002) The interaction between model resolution, observation resolution and observation density in data assimilation: a one-dimensional study. *Quarterly Journal of the Royal Meteorological Society*, 128, 1367–1386.
- Lukovich, J., Stroeve, J.C., Crawford, A., Hamilton, L., Tsamados, M., Heorton, H. and Massonnet, F. (2021) Summer extreme cyclone impacts on Arctic Sea ice. *Journal of Climate*, 34, 4817–4834. <https://doi.org/10.1175/JCLI-D-19-0925.1>.
- Mlawer, E.J., Taubman, S.J., Brown, P.D., Iacono, M.J. and Clough, S.A. (1997) Radiative transfer for inhomogeneous atmospheres: RRTM, a validated correlated-k model for the long-wave. *Journal of Geophysical Research*, 102, 16663–16682. <https://doi.org/10.1029/97JD00237>.
- Morrison, H., Thompson, G. and Tatarskii, V. (2009) Impact of cloud microphysics on the development of trailing stratiform precipitation in a simulated squall line: comparison of one- and two-moment schemes. *Monthly Weather Review*, 137, 991–1007.
- Nakanishi, M. (2001) Improvement of the Mellor–Yamada turbulence closure model based on large-eddy simulation data. *Boundary Layer Meteorology*, 99, 349–378.
- Nakanishi, M. and Niino, H. (2004) An improved Mellor–Yamada level-3 model with condensation physics: its design and verification. *Boundary Layer Meteorology*, 112, 1–31.
- Nakanishi, M. and Niino, H. (2006) An improved Mellor–Yamada level-3 model: its numerical stability and application to a regional prediction of advection fog. *Boundary Layer Meteorology*, 119, 397–407.
- Parrish, D.F. and Derber, J.C. (1992) The national meteorological center's spectral statistical-interpolation analysis

- system. *Monthly Weather Review*, 120, 1747–1763. [https://doi.org/10.1175/1520-0493\(1992\)120<1747:TNMCS>2.0.CO;2](https://doi.org/10.1175/1520-0493(1992)120<1747:TNMCS>2.0.CO;2).
- Pierrehumbert, R.T. and Swanson, K.L. (1995) Baroclinic instability. *Annual Reviews of Fluid Mechanics*, 27, 419–467.
- Rabier, F., Järvinen, H., Klinker, E., Mahfouf, J.-F. and Simmons, A. (2000) The ECMWF operational implementation of four-dimensional variational assimilation. I: experimental results with simplified physics. *Quarterly Journal of the Royal Meteorological Society*, 126, 1143–1170.
- Rawlins, F., Ballard, S.P., Bovis, K.J., Clayton, A.M., Li, D., Inverarity, G.W., Lorenc, A.C. and Payne, T.J. (2007) The met office global 4-dimensional data assimilation system. *Quarterly Journal of the Royal Meteorological Society*, 133, 347–362.
- Simmonds, I., Burke, C. and Keay, K. (2008) Arctic climate change as manifest in cyclone behavior. *Journal of Climate*, 21, 5777–5796.
- Skamarock, W.C., Klemp, J.B., Dudhia, J., Gill, D.O., Barker, D.M., Duda, M.G., Huang, X.Y., Wang, W. and Powers, J.G. (2008) *A Description of the Advanced Research WRF Version 3*, Vol. 475. Boulder, CO: NCAR Technical Note, p. 113. <https://doi.org/10.5065/D68S4MVH>.
- Steinhoff, D.F., Bromwich, D.H. and Monaghan, A.J. (2013) Dynamics of the foehn mechanism in the McMurdo dry valleys of Antarctica from polar WRF. *Quarterly Journal of the Royal Meteorological Society*, 139, 1615–1631. <https://doi.org/10.1002/qj.2038>.
- Tao, T., Zhang, J. and Zhang, X. (2017b) The role of stratosphere vortex downward intrusion in a long-lasting late-summer Arctic storm. *Quarterly Journal of the Royal Meteorological Society*, 143, 1953–1966. <https://doi.org/10.1002/qj.3055>.
- Tao, W., Zhang, J., Fu, Y. and Zhang, X. (2017a) Driving roles of tropospheric and stratospheric thermal anomalies in intensification and persistence of the Arctic superstorm in 2012. *Geophysical Research Letters*, 44, 10017–10025. <https://doi.org/10.1002/2017GL074778>.
- Wilson, A.B., Bromwich, D.H. and Hines, K.M. (2011) Evaluation of polar WRF forecasts on the Arctic system reanalysis domain: surface and upper air analysis. *Journal of Geophysical Research*, 116, D11112. <https://doi.org/10.1029/2010JD015013>.
- Wu, Y., Liu, Z. and Li, D. (2020) Improving forecasts of a record-breaking rainstorm in Guangzhou by assimilating every 10-min AHI radiances with WRF 4DVAR. *Atmospheric Research*, 239, 104912.
- Yamagami, A., Matsueda, M. and Tanaka, H.L. (2017) Extreme arctic cyclone in August 2016. *Atmospheric Science Letters*, 18, 307–314.
- Yamagami, A., Matsueda, M. and Tanaka, H.L. (2018a) Medium-range forecast skill for Arctic cyclones in summer of 2008–2016. *Geophysical Research Letters*, 45, 4429–4437. <https://doi.org/10.1029/2018GL077278>.
- Yamagami, A., Matsueda, M. and Tanaka, H.L. (2018b) Predictability of the 2012 great Arctic cyclone on medium-range timescales. *Polar Science*, 15, 13–23. <https://doi.org/10.1016/j.polar.2018.01.002>.
- Yanase, W. and Niino, H. (2007) Dependence of polar low development on baroclinicity and physical processes: an idealized high-resolution numerical experiment. *Journal of the Atmospheric Sciences*, 64, 3044–3067. <https://doi.org/10.1175/JAS4001.1>.

How to cite this article: Ban, J., Liu, Z., Bromwich, D.H. & Bai, L. (2023) Improved regional forecasting of an extreme Arctic cyclone in August 2016 with WRF MRI-4DVAR. *Quarterly Journal of the Royal Meteorological Society*, 149(757), 3490–3512. Available from: <https://doi.org/10.1002/qj.4569>

APPENDIX A

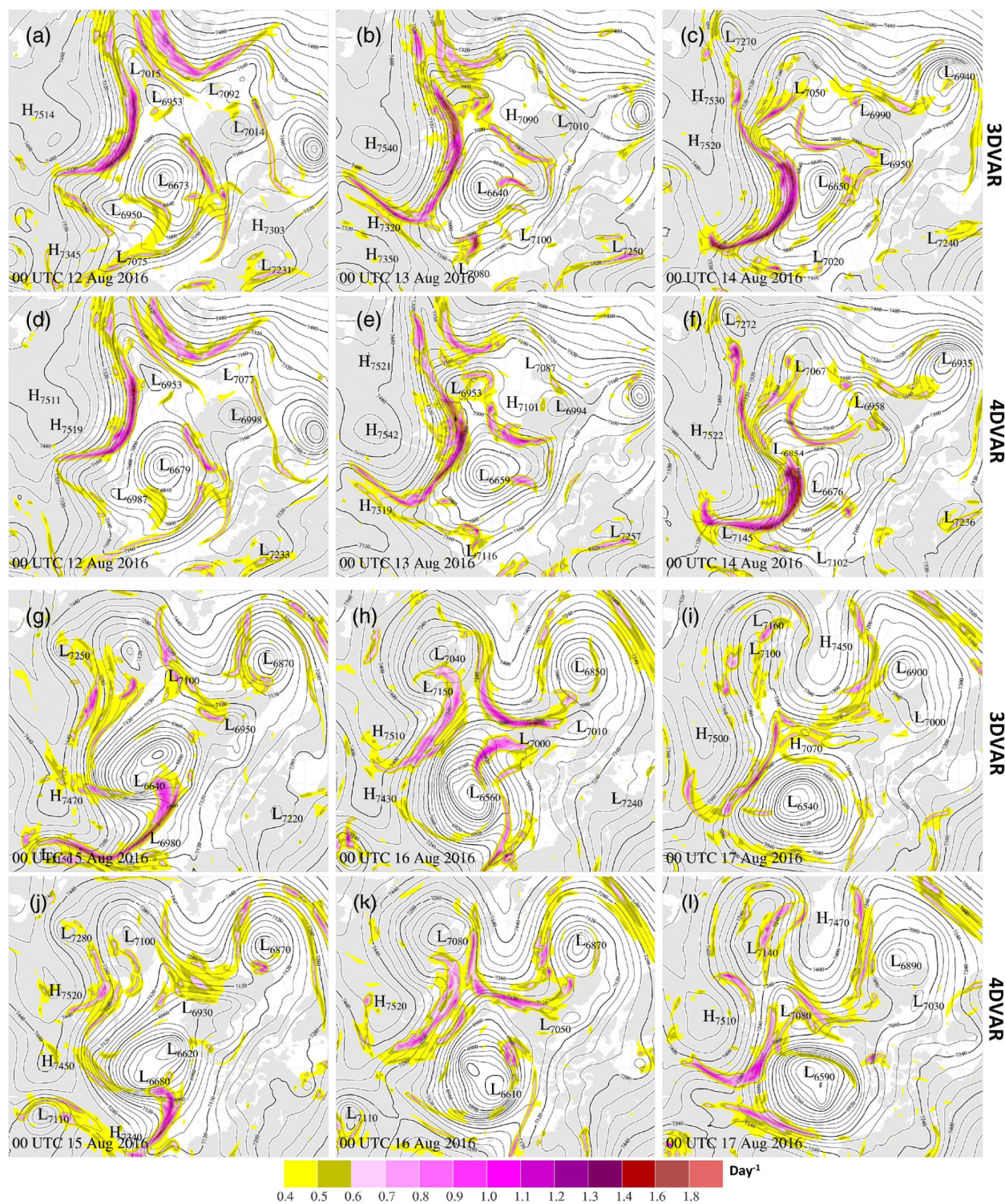


FIGURE A1 Geopotential height (black, on 400 hPa, contour interval is 40 geopotential meters) and Eady growth rate (shaded, day⁻¹, between 450 and 350 hPa) of the forecast initialized by 3DVAR and 4DVAR from 0000 UTC 12 August to 0000 UTC 17 August 2016. [Colour figure can be viewed at wileyonlinelibrary.com]